Faculty of Natural Science and Technology
Department of Physics

NTNU
Innovation and Creativity

MASTER'S THESIS FOR

STUD. TECHN. PAUL ANTON LETNES

Thesis started:	February 26, 2008
Thesis submitted:	July 15, 2008

DISCIPLINE: APPLIED PHYSICS

Norsk tittel:	*"Stråleskraping i SPS for LHC-injeksjon"* *Studier av effektivitet og robusthet*
English title:	*"Beam Scraping in the SPS for LHC Injection"* *Efficiency and Robustness Studies*

CERN-THESIS-2008-053
15/07/2008

This work has been carried out at CERN, under the supervision of Helmut Burkhardt.

Trondheim, July 15,

Jan Myrheim

Responsible supervisor

Professor at Department of Physics

Abstract

The Large Hadron Collider (LHC) at CERN will be the world's most powerful accelerator when it is commissioned in fall 2008. Operation of the LHC will require injection of very high intensity beams. Fast transverse beam scrapers have been installed in the Super Proton Synchrotron (SPS) injector to detect and, if necessary, remove transverse beam tails. This will help to both diagnose and prevent beam quenches in the LHC.

Scraping of a high intensity beam at top energy can potentially damage the scraper jaws. This has been studied with Monte Carlo simulations to find energy deposition and limits for hardware damage. Loss maps from scraping have been generated both with machine studies and tracking simulations.

Time dependent Beam Loss Monitor (BLM) measurements have shown several interesting details about the beam. An analytical model of time dependent losses is compared with beam measurements and demonstrates that beam scraping can be used to estimate the beam size. Energy deposition simulations also give the time dependence of scraping, and are compatible with measurements in this respect.

Several machine studies have been conducted to investigate transverse beam tails and possible uses of the beam scrapers. These have shown that the beam scrapers in combination with BLMs are very sensitive detectors of transverse beam tails. Measurements with coasting beam have shown that tails repopulate after some time. The most recent results from machine studies are discussed, in light of possible sources of tail repopulation.

Preface

This report was written as a master thesis for my master's degree at the Norwegian University of Science and Technology (NTNU), during spring 2008. The work associated with the report was done during my stay at CERN as a technical student. My work was related to many aspects of the SPS beam scrapers, from control application development to hardware protection and beam physics simulations. The main goal of this report is to show the results from this work, given as a technical student assignment.

The introductory chapters of the report are mainly aimed at readers from NTNU, to give some insight in the background of this work and the beautiful theory of particle motion in synchrotrons. CERN readers will be more interested in the chapters on robustness of the scrapers and scraping efficiency.

A conference paper has been published on this work, giving a summary of the most important results [1].

Contents

List of Figures

1 Introduction

This chapter will briefly explain the background for this work. The need for a beam scraper in the SPS is explained. Also, a short introduction to the underlying physics is given.

1.1 CERN and the LHC Project

CERN (English: European Organization for Nuclear Research), an international research institution, is the biggest particle physics lab in the world. It is located near Geneva, Switzerland, and was founded by 12 European countries in 1959. Always striving for the discovery of new and ever more exotic particles, CERN has hosted many large particle accelerators.

At present, the completion of the Large Hadron Collider (LHC) is CERN's top priority. Four large (and some small) experiments located in four of the eight Interaction Regions (IRs) of the LHC ring will study proton-proton and ion-ion collisions. The LHC will be extraordinary in many ways: a storage ring 27 km in circumference, a maximal proton momentum of 7 TeV/c, and a main dipole bending field of more than 8 T are all impressive feats. The successful commissioning of the LHC relies on the use of a large number of new and innovative technologies.

1.2 Superconducting Magnets

A key technology for the LHC is superconducting magnet technology. For example, all the 1232 main bending dipoles in the LHC are superconducting. The superconductor itself consists of thin niobium-titanium wires embedded in a copper matrix. This material is superconducting only under very special conditions: for each value of magnetic field and current density, there is an upper limit on temperature. For the LHC, the nominal operating temperature of the magnets is 1.9 K, obtained by superfluid helium cooling. Local heating above this temperature may lead to loss of superconducting ability. A consequence of this is electrical resistance, which in turn leads to more heating.

To avoid this undesired avalanche effect (and any subsequent hardware damage), known as a magnet quench, several protection systems have been implemented. One of these is the LHC collimation system, which removes protons with large oscillation amplitude from the beam (known as beam halo). This is done to prevent magnet heating caused by beam losses, i.e. protons impacting the beam pipe and causing local heating.

As the beam collimation insertions in the LHC are several kilometers from the point of beam injection, the collimation system is not able to prevent quenches during the first part of the injection phase. Estimates show that the nominal SPS beam intensity for LHC injection exceeds the magnet quench limit by nearly four orders of magnitude [2]. Hence, an important goal is to inject only beams with virtually no high amplitude halo. To achieve this goal, fast beam scrapers have been installed in the Super Proton Synchrotron (SPS), the LHC injector.

1.3 The Injector Chain

Before looking at the SPS, a word on the injector chain is in order. LHC injection imposes challenging requirements on the injector chain [3]. A schematic map of the CERN accelerators is shown in Figure 1.1. For the current discussion, the most important particle species is the proton: colliding protons is the main objective of the LHC.

Initially, protons are extracted from a tank of hydrogen. The first step of acceleration is done by LINear ACcelerator 2 (LINAC2). The protons are then injected into the Proton Synchrotron Booster (PSB). After being accelerated to a particle momentum of 2.1 GeV/c, the beam is injected into the Proton Synchrotron (PS) itself.

Commissioned in 1959, it is the oldest of the currently used particle accelerators at CERN. It was also CERN's first big accelerator project. For LHC injection, the PS injects a beam with a momentum of 26 GeV into the SPS. Being a 6.9 km circumference synchrotron commissioned in 1976, the SPS has been used for several purposes: proton-antiproton collider, delivery of beams for fixed target experiments, and injector to the Large Electron Positron (LEP) collider. Starting fall 2008, the SPS will inject beams into the LHC.

1.4 The SPS and the Beam Scrapers

The SPS will be the final pre-accelerator for the LHC, accelerating protons from the injection momentum of 26 GeV/c to 450 GeV/c. Being a ring accelerator, allowing for multiple passes through the scraper, it is more convenient to perform the beam scraping in the SPS than in a single pass transfer line. The current scheme involves scraping the beam at top energy, immediately before injecting the beam into the LHC. Scraping at 3.5 σ is foreseen to prevent quenches due to injection losses [4] (σ is here the nominal RMS beam size). The scrapers, when used together with Beam Loss Monitors (BLM), are also sensitive detectors of beam tails, giving the possibility of dumping the beam, instead of injecting it, if the beam is too dirty. Before injection into the LHC, many beam parameters have to be checked to ensure good beam quality [5].

The beam scrapers themselves consist of two copper jaws, one for each transverse plane. Two stepping motors control the position of the jaws. In terms of size, the jaws have an active length of 30 mm (along the beam axis), and a transversal width of 12 mm. Figure 1.2 shows the scraper jaws in the beam pipe.

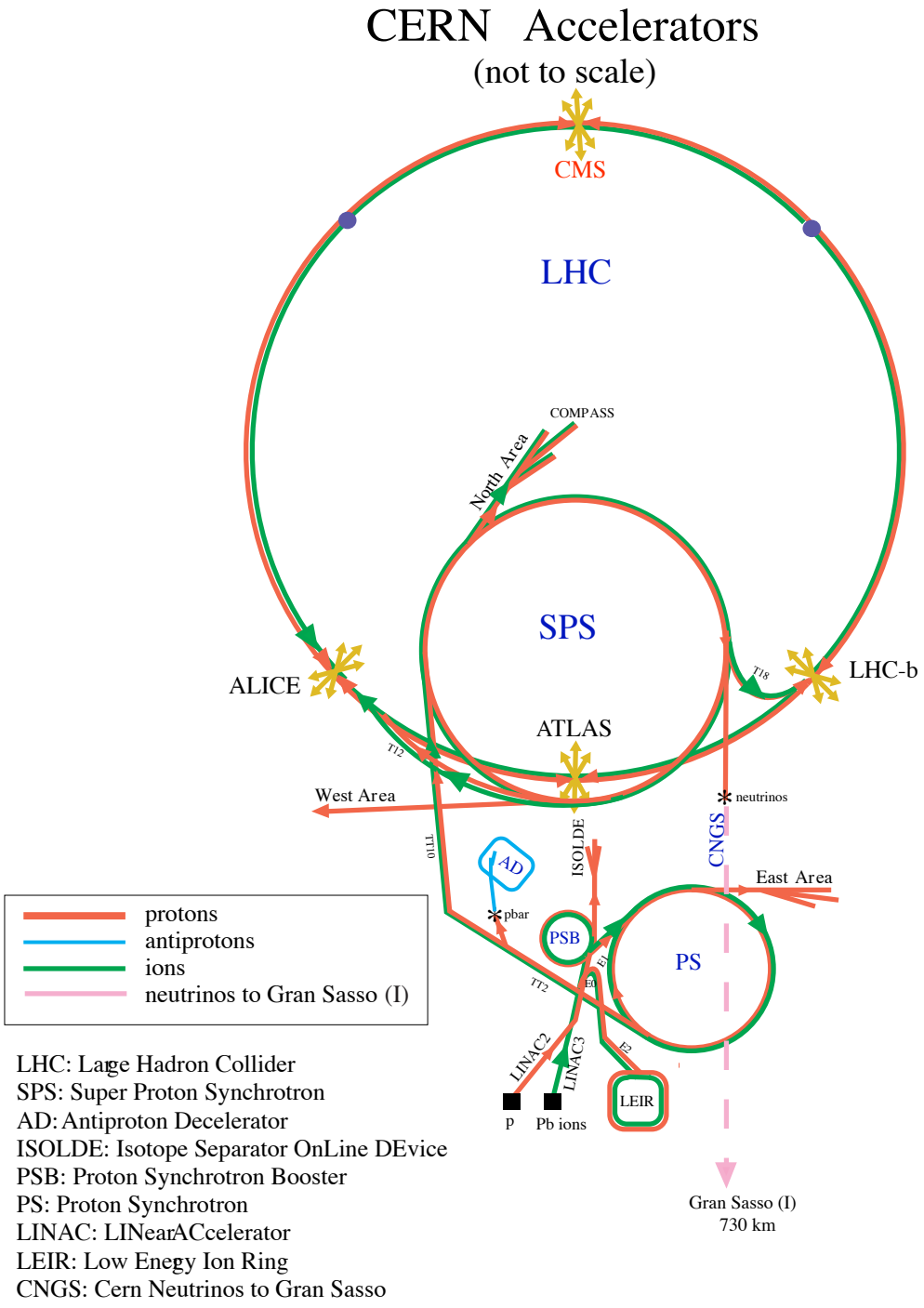

Figure 1.1: The CERN accelerator complex. Figure: R. Ley.

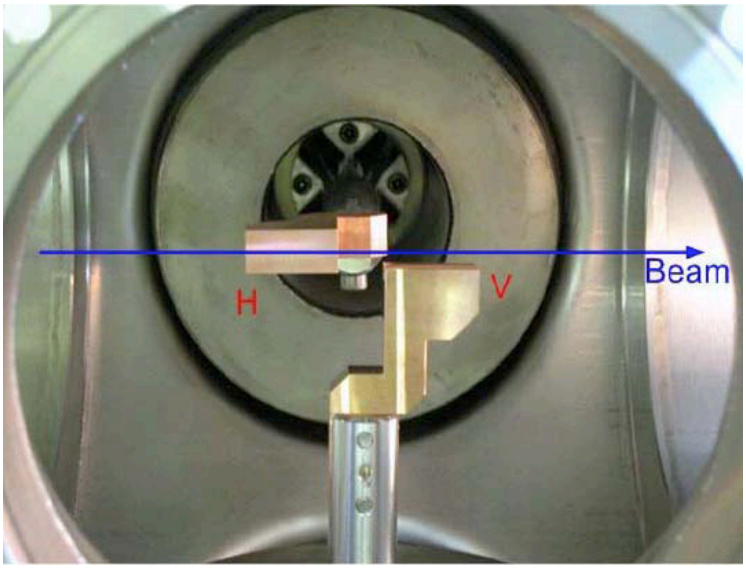

Figure 1.2: The copper jaws of the beam scrapers, installed in the SPS.

The beam scrapers have been installed in the SPS Long Straight Section 5 (LSS5). They are connected to a Front End Computer (FEC) running a FESA server, which is the "user interface" for writing high level control software. For regular operation, a high level Java application built on top of the `cern.japc` framework is written and run in the CERN Control Centre (CCC). This application communicates settings and status to and from the FEC. A more detailed discussion of how the scrapers are controlled can be found in [6].

1.5 Use of the Transverse Beam Scrapers

An overview of how the horizontal scraper jaw moves relative to the SPS beam is given in Figure 1.3. For each transverse plane, a scraping position is given. This position decides how much of the beam is scraped. In addition, the parking and out positions are set to the same value for both planes. The vertical movement is a fast sweep with no precision control; the jaw moves from the lower to the upper end switch. Horizontally, the movement is controlled by a precise stepping motor. The time of the scraping is set by the SPS operator from the high level application, but all other timing is controlled from the low level FESA server.

The horizontal scraper moves according to the following pattern:

1. The jaw moves horizontally from its parking position to the scraping position set by the operator, point 1
2. Scraping is conducted by a quick, vertical sweep to point 2
3. The jaw moves out to point 3, given by the operator as a horizontal distance from point 2

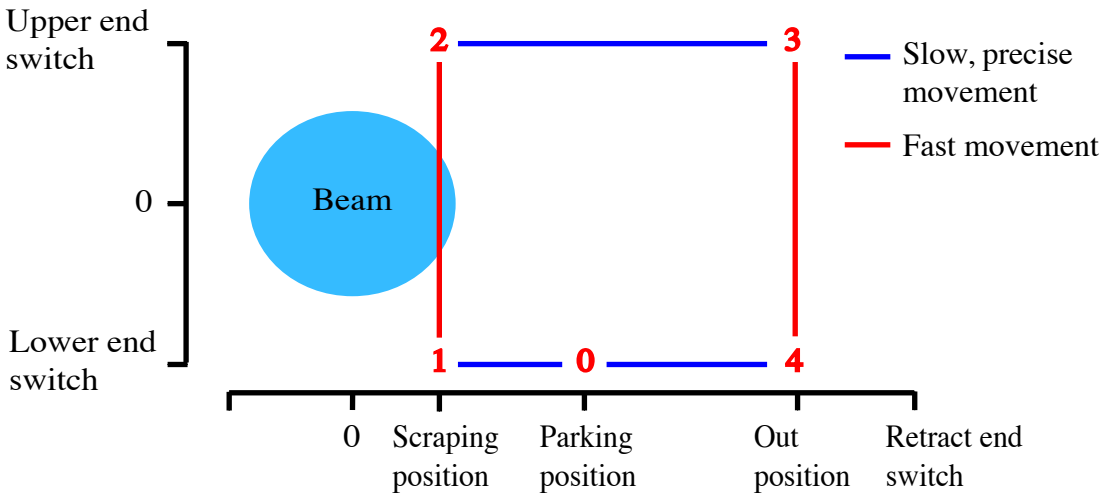

Figure 1.3: Movement of the scraper jaw relative to the beam. Note that the scraper always sweeps quickly through the beam, and is never left in the beam over time. Only the horizontal plane is shown here.

4. The jaw moves down to point 4
5. The jaw moves to its parking position, point 0, and waits for the next user cycle with scraping

The speed of the fast scraper sweep is 0.20 m/s [7].

If the scrapers are not being used, they should be retracted to the retract end switch. Here, the SPS interlock system prevents unintentional scraping of the beam. If the scraper jaws start moving, the interlock will dump the beam. For more details on how the scrapers work and are controlled, see [6].

As the beam position is not known a priori, it is necessary to measure it before scraping high intensities. This can be done using the scrapers themselves. By injecting a low intensity beam, one can scrape closer and closer to the beam center until the whole beam is removed. In this manner, the beam position and the beam size can be determined in both transversal planes. As the SPS orbit is very stable, scraping can now be performed in a reproducible manner [2]. With good knowledge of beam position and size, one can set a scraping position in beam σ which will ensure protection of the LHC cold aperture.

1.6 Scraper-Beam Interaction

There are three main interaction mechanisms between beam protons and the jaw:

- Multiple scattering
- Nuclear interactions
- Electromagnetic stopping power

It is useful to look at some quantitative estimates of the strength of each effect, to understand how important these mechanisms are for removing protons from the beam.

1.6.1 Multiple Scattering

Multiple scattering of charged particles in matter is mainly caused by Coulomb scattering between the particles in question (here, protons) and the nuclei of the material. There is also a small strong interaction contribution. For small scattering angles, which is the most likely case at high energy, the scattering cross section is approximately Gaussian with an RMS width of

$$\theta_0 = \frac{13.6\ \text{MeV}}{\beta cp} z\sqrt{x/X_0}\left[1 + 0.038 \ln\left(x/X_0\right)\right]. \tag{1.1}$$

Here, βc is the impinging particle's velocity, p the momentum, z the charge number, and x/X_0 the material's thickness in radiation lengths. Copper has $z = 29$ protons and a radiation length of $X_0 = 1.44$ cm. For protons with $pc = 450$ GeV, this yields an RMS scattering angle of $\theta_0 = 45$ µrad. This is of the same order of magnitude as the RMS betatron oscillation angle of beam protons, meaning that multiple scattering has an important effect on beam protons.

The data and formulas for these calculations are given in [8].

1.6.2 Nuclear Interactions

Inelastic nuclear interactions between protons and copper give an important contribution to scraping efficiency. The nuclear interaction length of copper is 153 mm [8]. Given the interaction probability

$$P_I(x) = 1 - \mathrm{e}^{-x/\lambda_I}, \tag{1.2}$$

where x is the length of material traversed and λ_I is the interaction length, we find that for one passage, the interaction probability is 0.178. We will assume that a nuclear interaction will instantly remove the proton from the beam. It should be noted that particle showers from nuclear interactions deposit a lot of energy in the copper, and could cause melting of the jaw. This will be discussed in greater detail in chapter 3.

Let us also calculate the average number of passes a proton has through the jaw before it is removed from the beam, assuming that nuclear interaction is the only relevant mechanism. For each pass through the jaw, there is a $q = 1 - 0.178 = 0.822$ probability of survival. The probability of n passes through the jaw is

$$P_s(n) = q^n. \tag{1.3}$$

The average number of passes is then

$$\langle n \rangle = \sum_{i=0}^{\infty} q^i = \frac{1}{1-q} = 5.62, \tag{1.4}$$

where we have used the formula for the sum of a geometric series. As this is a relatively small number, we can assume that nuclear interactions will be an important mechanism for beam cleaning.

1.6.3 Stopping Power

The average stopping power $(-\mathrm{d}E/\mathrm{d}x)$ for $pc = 450$ GeV protons in copper is 54 MeV [8]. If we assume the average number of passes through the jaw given by Equation (1.4), the average energy loss is 301 MeV. This number is smaller than the maximal stable amplitude for synchrotron motion (known as the RF bucket height, see Chapter 2.2). In terms of beam cleaning, this means that the slowing down of protons in the copper jaw is too small to remove a significant fraction of scraped protons from the beam. This effect will not be of great importance when scraping.

1.6.4 Beam Energy

The nominal SPS proton beam for LHC injection consists of 288 bunches, each containing around $1.15 \cdot 10^{11}$ protons with a momentum of 450 GeV/c [9]. This gives a total beam energy of 2.39 MJ, enough to melt several kilograms of copper initially at room temperature. Given that the scraper jaws are small, with an active length of 30 mm, not all of this energy will be deposited inside the scraper. However, a more thorough investigation of robustness of the hardware is in order, to determine whether scrapers can be damaged during scraping.

1.7 Issues to Investigate

At the beginning of this work, several issues regarding beam scraping had to be understood in more detail. The perhaps most important issue was hardware robustness: Can the scraper itself, or downstream lattice elements, be damaged when scraping high intensity beams? Answering this question is both important and nontrivial.

Other, more academic questions have also arisen. In previous Machine Development sessions (MDs) [2], tail (or beam halo) repopulation has been observed. Briefly explained, this is the following process:

1. The beam is scraped at a certain σ
2. Beam losses are observed because of the scraping process
3. After some time, the beam is again scraped at the same σ
4. Beam losses are observed again

Or, in other words, low amplitude protons are somehow scattered out to higher amplitudes as time goes by. The most striking feature of the observations is that there is a large tail repopulation in the horizontal plane, while there is little or no repopulation in the vertical plane. Tail repopulation is observed to be a stable, reproducible and continuous process.

Another question one can ask is the following: what does the time dependence of scraping look like, and what can we learn from it? Measured time dependent beam

losses can give insight as to how efficient scraping is, and which interaction mechanisms are the most important. These beam loss measurements can also be used to estimate beam properties like the beam size.

2 Theory of Synchrotron Particle Motion

This chapter will explain the theory of particle motion in a synchrotron. The theory presented is necessary to understand the scraper's effect on the beam. Only the concepts necessary for the discussion regarding beam scraping will be explained in detail.

2.1 Transversal Particle Motion

Particles in particle accelerators always have a small oscillation, known as the betatron oscillation, around the design orbit. In this chapter, the linear theory of such motion is introduced. With this theory, one can understand the effect of scrapers on the beam.

2.1.1 A Convenient Coordinate System

The force governing a proton's motion in electromagnetic fields is the well-known Lorentz force,

$$\frac{\mathrm{d}\vec{p}}{\mathrm{d}t} = e(\vec{E} + \vec{v} \times \vec{B}). \tag{2.1}$$

By expressing $\vec{E}$ and $\vec{B}$ in terms of the vector potential $\vec{A}$ and the scalar potential Φ,

$$\begin{aligned}\vec{E} &= -\nabla\Phi - \partial\vec{A}/\partial t,\\ \vec{B} &= \nabla \times \vec{A},\end{aligned}$$

the Hamiltonian for particle motion is given by

$$\mathcal{H} = e\Phi + c\left[m^2c^2 + \left(\vec{P} - e\vec{A}\right)^2\right]^{1/2}. \tag{2.2}$$

Here, $\vec{P}$ is the canonical momentum with $\vec{P} = \vec{p} + e\vec{A}$, where $\vec{p}$ is the mechanical momentum. The equations of motion are now

$$\dot{x} = \frac{\partial\mathcal{H}}{\partial P_x}, \quad \dot{P}_x = -\frac{\partial\mathcal{H}}{\partial x}.$$

The formulation is not yet very useful, as it does not exploit any symmetries or properties of the system's geometry. Rather than a standard cartesian coordinate system,

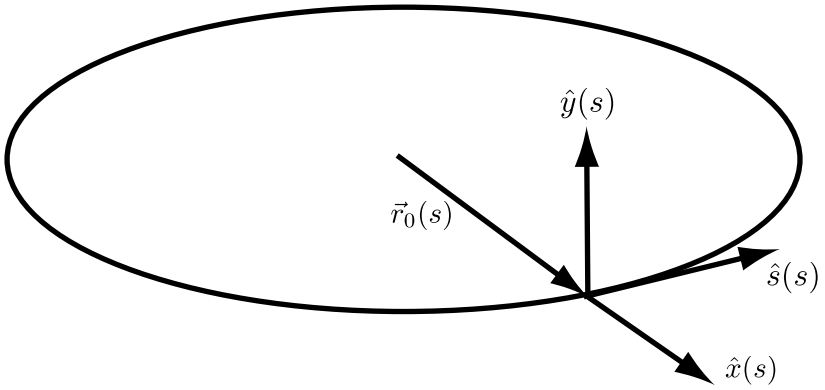

Figure 2.1: Frenet–Serret curvilinear coordinate system used for transverse beam dynamics analysis.

a curvilinear Frenet–Serret coordinate system is used to describe particle motion in particle accelerators. The coordinate system is shown in Figure 2.1.

The basis for this coordinate system is $\vec{r_0}(s)$, the reference orbit. The reference orbit is normally designed to pass through the center of the magnetic elements. The three coordinates used are x, y and s. s is the length along the curve $\vec{r_0}(s)$, measured from a chosen initial starting point. s is positive along the unit vector

$$\hat{s}(s) = \frac{\mathrm{d}\vec{r_0}(s)}{\mathrm{d}s},$$

which is the tangent vector of the reference orbit $\vec{r_0}(s)$.

x and y are, respectively, the horizontal (positive direction out of the ring) and vertical (positive direction upwards) particle coordinates. x and y locally form a plane orthogonal to $\hat{s}(s)$ (z will be used as a substitute for any of the two coordinates x and y where the treatment of x and y is equal). The unit vectors can be expressed as, respectively,

$$\begin{aligned}\hat{x}(s) &= -\rho(s)\frac{\mathrm{d}\hat{s}(s)}{\mathrm{d}s},\\ \hat{y}(s) &= \hat{x}(s) \times \hat{s}(s).\end{aligned}$$

Here, $\rho(s)$ is the local radius of curvature. With these formulas in hand, we describe the particle trajectory $\vec{r}(s)$ relative to the reference orbit:

$$\vec{r}(s) = \vec{r}_0(s) + x\hat{x}(s) + y\hat{y}(s).$$

The Hamiltonian in Equation (2.2) can now be transformed to this coordinate system. This is done by a canonical transformation. In the small angle approximation, the Hamiltonian can also be linearized. The result is found in [10]:

$$H \approx -p\left(1+\frac{x}{\rho}\right) + \frac{1+x/\rho}{2p}\left[(p_x - eA_x)^2 + (p_y - eA_y)^2\right] - eA_s. \tag{2.3}$$

Here, $\mathcal{H} - e\Phi = E$ is the total particle energy and $p = \sqrt{E^2/c^2 - m^2c^2}$ is the total particle momentum. The conjugate phase space coordinates are now $(x, p_x; y, p_y; t, -\mathcal{H})$. We will only consider the transversal coordinates (x, y) and their conjugate momenta for now, leaving the treatment of longitudinal movement for later.

2.1.2 Magnetic Fields

In accelerator applications, we choose $\Phi = 0$, as there are no electrical fields present in the accelerator.[1] Furthermore, we approximate the magnetic fields as purely transversal to the particle motion, and can assume $A_x = A_y = 0$. Our two-dimensional magnetic field can be written as

$$\vec{B} = B_x(x, y)\hat{x} + B_y(x, y)\hat{y}.$$

We can write $\vec{B}$ in terms of the vector field:

$$B_x = -\frac{1}{1 + x/\rho}\frac{\partial A_s}{\partial y}, \quad B_y = \frac{1}{1 + x/\rho}\frac{\partial A_s}{\partial x}.$$

Inserting this result into Maxwell's famous equation $\nabla \times \vec{B} = 0$ yields

$$\frac{\partial}{\partial y}\frac{1}{1 + x/\rho}\frac{\partial A_s}{\partial y} + \frac{\partial}{\partial x}\frac{1}{1 + x/\rho}\frac{\partial A_s}{\partial x} = 0. \tag{2.4}$$

For large ρ, we can approximate $1 + x/\rho \approx 1$. A_s can be expanded as (see [10])

$$A_s = B_0 \Re\left[\sum_{n=1}^{\infty} \frac{b_n + \mathrm{i}a_n}{n}(x + \mathrm{i}y)^n\right].$$

Note that i is the imaginary unit. The complex representation for magnetic fields in two dimensions is called the Beth representation. A common convention is to set B_0 to the main dipole field strength.

Using Equation (2.4), we find the magnetic field strength to be

$$B_y + \mathrm{i}B_x = B_0 \sum_{n=1}^{\infty}(b_n + \mathrm{i}a_n)(x + \mathrm{i}y)^{n-1}, \quad \text{with}$$

$$b_n = \frac{1}{B_0(n-1)!}\frac{\partial^{n-1}B_y}{\partial x^{n-1}}\bigg|_{x=y=0} \quad \text{and} \quad a_n = \frac{1}{B_0(n-1)!}\frac{\partial^{n-1}B_x}{\partial x^{n-1}}\bigg|_{x=y=0}.$$

The naming convention is that b_n and a_n are called the $2n$th multipole coefficients, with dipole b_1, dipole roll a_1, quadrupole b_2, skew quadrupole b_2, and so on for sextupoles, octupoles etc.

[1] For the time being, we disregard the accelerating RF cavities, which are small, localized, and interfere only marginally with transverse motion.

2.1.3 Equation of Betatron Motion

From the Hamiltonian in Equation (2.3), we can now find the equations of motion:

$$x' = \frac{\partial H}{\partial p_x} = \left(1 + \frac{x}{\rho}\right)\frac{p_x}{p}, \quad p_x' = -\frac{\partial H}{\partial x} \approx \frac{p}{\rho} + eB_y, \tag{2.5}$$

$$y' = \frac{\partial H}{\partial p_y} = \left(1 + \frac{x}{\rho}\right)\frac{p_y}{p}, \quad p_y' = -\frac{\partial H}{\partial y} = -eB_x, \tag{2.6}$$

where we neglect terms of $\mathrm{O}(x^2)$ and $\mathrm{O}(p_x^2)$. We use the notation $x' = \mathrm{d}x/\mathrm{d}s$.

We will also approximate the magnetic fields B_x and B_y by a linear approximation starting from the reference orbit:

$$B_x = y\frac{\partial B_y}{\partial x}\bigg|_{x=y=0}, \quad B_y = -B_0 + x\frac{\partial B_y}{\partial x}\bigg|_{x=y=0}.$$

Inserting the approximations for the magnetic fields and rewriting Equation (2.5) and (2.6) as two second-order ordinary differential equations, we get Hill's equations of betatron motion:

$$x'' + K_x(s)x = 0, \quad K_x(s) = \frac{1}{\rho^2} - K_1(s) \quad \text{and} \tag{2.7}$$

$$y'' + K_y(s)y = 0, \quad K_y(s) = K_1(s) \tag{2.8}$$

where

$$K_1(s) = \frac{\partial B_y}{\partial x}\bigg|_{x=y=0}$$

is known as the "effective focusing function".[2] On this form, we recognize the equations of motion as a special case of Hill's equation. These equations are subject to a lot of approximations. However, they are well suited to demonstrate particle motion in bending magnets and focusing magnets. When these approximations are made, it is referred to as linear or first order optics. For short time scales, which we typically have during scraping, linear optics is sufficient to analyze the beam's behavior.

2.1.4 The Main Magnetic Elements: Dipoles and Quadrupoles

The two most important magnetic elements in a strong focusing synchrotron are dipoles, or bending magnets, and quadrupoles, or focusing magnets. In a perfect dipole, the magnetic field is a homogeneous vertical field, which will bend charged particles into a circular orbit according to Equation (2.1). Quadrupoles either focus or defocus the particles relative to the reference orbit. The quadrupoles are thus used to control the local beam size.

[2] In some literature, one quotes the focusing index $n(s) = \rho K_1(s)$. For weak focusing synchrotrons, who use edge focusing and other weak focusing effects, $0 \leq n(s) \leq 1$. For alternating gradient (or "strong focusing") synchrotrons, $|n(s)| > 100$.

In a dipole, we have $K_x(s) = 1/\rho^2$, $K_y(s) = 0$. This means that the horizontal particle movement corresponds to a harmonic oscillator, while the vertical particle movement is a straight line ($y'' = 0$). Note that this is only the case for sector dipoles, where the entrance and exit particle trajectories are perpendicular to the edge of the dipole magnet. For rectangular dipoles, one has an edge focusing or defocusing effect, exploited in weak focusing synchrotrons. See [10] for a discussion.

In quadrupoles, we have $1/\rho = 0$, and $K_x = -K_y \approx$ constant. This focuses the beam in one plane and defocuses in the other. In an accelerator lattice, several focusing and defocusing quadrupoles are combined to get a net focusing effect. As a convention, quadrupoles which focus in the horizontal plane are called focusing quadrupoles, while vertically focusing quadrupoles are called defocusing quadrupoles.

2.1.5 Transfer Matrices

Because well made accelerator components have close to idealized fields, the focusing function $K_1(s)$ is approximately piecewise constant. We now let z, z' be one of the two transverse coordinates and its derivative with respect to s. We then compactly write Equations (2.7) and (2.8) as

$$z'' + K_z(s)z = 0. \tag{2.9}$$

The solutions of Hill's equation with piecewise constant K_z are combinations of the following functions:

$$\begin{cases} a\cos\left(\sqrt{K_z}s + b\right), & K_z > 0, \\ as + b, & K_z = 0, \\ a\cosh\left(\sqrt{-K_z}s + b\right), & K_z < 0. \end{cases}$$

Here, a and b are integration constants determined by the initial conditions. Because of the linear nature of these equations, we can express the solution to Hill's equation as a linear transformation of the initial condition:

$$\mathbf{z}(s) = M(s|s_0)\mathbf{z}(s_0),$$

where $\mathbf{z}$ is the betatron state vector,

$$\mathbf{z}(s) = \begin{pmatrix} z(s) \\ z'(s) \end{pmatrix}.$$

We call $M(s|s_0)$ the transfer matrix from s_0 to s.

The transfer matrices for ideal quadrupoles of length l are:

$$M(s|s_0) = \begin{cases} \begin{pmatrix} \cos\sqrt{K}l & \frac{1}{\sqrt{K}}\sin\sqrt{K}l) \\ -\sqrt{K}\sin\sqrt{K}l & \cos\sqrt{K}l \end{pmatrix} & K > 0\text{: focusing quad.} \\ \begin{pmatrix} 1 & l \\ 0 & 1 \end{pmatrix} & K = 0\text{: drift space.} \\ \begin{pmatrix} \cosh\sqrt{|K|}l & \frac{1}{\sqrt{|K|}}\sinh\sqrt{|K|}l \\ \sqrt{|K|}\sinh\sqrt{|K|}l & \cosh\sqrt{|K|}l \end{pmatrix} & K < 0\text{: defocusing quad.} \end{cases}$$

In the thin lens approximation, $l \to 0$, these matrices reduce to thin lens transfer matrices on the form

$$M_{\text{focusing}} = \begin{pmatrix} 1 & 0 \\ -1/f & 1 \end{pmatrix},$$

with f being the focal length given by

$$f = \lim_{l \to 0} \frac{1}{Kl}.$$

For a pure sector dipole ($K_x = 1/\rho^2$), the transfer matrices are

$$M_x(s|s_0) = \begin{pmatrix} \cos\theta & \rho \sin\theta \\ -\frac{1}{\rho}\sin\theta & \cos\theta \end{pmatrix}$$

with $\theta = l/\rho$ and M_y is the transfer matrix of a drift space. The asymmetry between M_x and M_y is of course because ideal dipoles only bend in the horizontal plane. For a large accelerator, ρ is large and θ is small, making the horizontal transfer matrix of a dipole approximately equal to the transfer matrix of a drift space.

The transfer matrix $M(s|s_0)$ is now just the product of the transfer matrices of all the elements between s and s_0. Hence, the equations of motion are now solved if the transfer matrices of each lattice element can be established.

Transfer Matrices and Linear Stability

For stability analysis, we will look at the transfer matrix of a periodic lattice with a period of length L, $\mathbf{M}(s) = M(s + L|s)$. The most important example of this is an accelerator ring, in which we call $\mathbf{M}(s)$ the one turn matrix. The transfer matrix for k turns is $[\mathbf{M}(s)]^k$. We are only interested in lattices in which the accelerated particles have an upper limit on their oscillation amplitude, even after many turns. In other words, the matrix elements have to stay bounded for large k.

The condition for this can be found by the following argument. The eigenvalue equation for $\mathbf{M}$ is

$$\begin{aligned} |\mathbf{M} - \lambda \mathbb{I}| = 0, \text{ or} \\ \lambda^2 - \lambda(a + d) + 1 = 0, \end{aligned} \tag{2.10}$$

if we make use of the fact that Det $(\mathbf{M}) = ad - bc = 1$. This property follows from the fact that Equation (2.9) has no first derivative term. $a, b, c,$ and d are here the four matrix elements of $\mathbf{M}$. We now define μ, which we will denote as the one-turn phase advance, as

$$\cos\mu = \frac{1}{2}\ \text{Tr}\ (\mathbf{M}) = \frac{1}{2}(a + d). \tag{2.11}$$

This makes the two solutions to (2.10)

$$\lambda = \cos\mu \pm \mathrm{i}\sin\mu = \mathrm{e}^{\pm \mathrm{i}\mu}.$$

Note that μ is real if $|a+d| \leq 2$, and complex if $|a+d| > 2$.

Let us assume that $a+d \neq 2$. Then M can be parametrized in terms of the Courant–Snyder parameters α, β and γ in [11]:

$$\begin{aligned} a - d &= 2\alpha \sin\mu, \\ b &= \beta \sin\mu, \\ c &= -\gamma \sin\mu. \end{aligned}$$

Note that none of the Courant–Snyder parameters, α, β, γ, are related to relativistic factors. The condition $\mathrm{Det}(\mathbf{M}) = 1$ becomes

$$\beta\gamma - \alpha^2 = 1.$$

We can now write the matrix $\mathbf{M}$ as

$$\mathbf{M} = \mathbb{I}\cos\mu + \mathbb{J}\sin\mu \tag{2.12}$$

where $\mathbb{I}$ is the identity matrix and $\mathbb{J}$ is

$$\mathbb{J} = \begin{pmatrix} \alpha & \beta \\ -\gamma & -\alpha \end{pmatrix}.$$

If we examine the transfer matrix at two positions s_1 and s_2, we find that they are related by a similarity transform:

$$\begin{aligned} M(s_2 + L|s1) = \mathbf{M}(s_2)M(s_2|s_1) &= M(s_2|s_1)\mathbf{M}(s_1), \\ \mathbf{M}(s_2) &= M(s_2|s_1)\mathbf{M}(s_1)M(s_2|s_1)^{-1}. \end{aligned}$$

This means that the trace of $\mathbf{M}(s)$ (and hence μ) is the same for all s since similar matrices have the same trace.

For the stability analysis, we note that

$$(\mathbb{I}\cos\mu_1 + \mathbb{J}\sin\mu_1)(\mathbb{I}\cos\mu_2 + \mathbb{J}\sin\mu_2) = \mathbb{I}\cos(\mu_1+\mu_2) + \mathbb{J}\sin(\mu_1+\mu_2),$$

and the k'th power of $\mathbf{M}$ is thus

$$\mathbf{M}^k = (\mathbb{I}\cos k\mu + \mathbb{J}\sin k\mu).$$

We now understand that if μ is real, particles will oscillate with an amplitude that does not grow in time. The (linear) stability condition on $\mathbf{M}$ is thus that $|a+d| < 2$.

SPS Single Turn Transfer Matrix

It is useful to know the single turn transfer matrix for the SPS at the position of the beam scrapers. The beam scrapers are installed at the position $s = 5136.09$ m in the SPS ring, in "Long Straight Section 5" (LSS5). Using the beam parameters from Table 3.1 and Table 3.2, and Equation (2.12), we find the horizontal transfer matrix to be

$$\mathbf{M}_x(s = 5136.08\text{ m}) = \begin{pmatrix} 1.77 & 38.27\text{ m} \\ 0.0447\text{ m}^{-1} & -0.402 \end{pmatrix}. \tag{2.13}$$

The transfer matrix in the vertical plane can be found in the same way.

2.1.6 Betatron Oscillation Amplitude

Courant and Snyder suggested the following function as a solution to the equations of motion:

$$z(s) = aw_z(s)\mathrm{e}^{\mathrm{i}\Phi_z(s)}. \tag{2.14}$$

Here, a is a constant yet to be specified. We denote Φ as the phase advance and w as the envelope function of betatron oscillation. Inserting Equation (2.14) into Equation (2.9) gives the equations for w and Φ:

$$\begin{aligned} w'' + Kw - \frac{1}{w^3} &= 0, \\ \Phi' &= \frac{1}{w^2}. \end{aligned}$$

By comparing this solution to the one turn transfer matrix, $M(s_2|s_1) = M(s_1 + L|s_1)$, we obtain the following relationships:

$$\begin{aligned} \Phi(s_2) - \Phi(s_1) &= \mu, \\ w^2 &= \beta, \\ ww' &= -\alpha. \end{aligned}$$

This is valid if we can show that $\beta^{1/2}$ is a periodic solution to Equation (2.9), and that $\beta' = -2\alpha$. This is shown in [11]. It is relevant to note that the envelope function β gives name to "betatron oscillation" and similar names.

An important result here is the relationship between β and Φ:

$$\Phi_z(s) = \int_0^s \frac{\mathrm{d}s}{\beta_z}, \tag{2.15}$$

and $\mu_z = \Phi_z(L)$. We will from now on take this to be the definition of μ and Φ, as Equation (2.11) only defines μ modulo 2π.

a is called the Courant–Snyder invariant, and is a conserved quantity. a is also sometimes called the "single-particle emittance". Usually, the emittance is defined as an RMS quantity which determines the beam size, see Chapter 2.1.8.

2.1.7 Dispersion and Chromaticity

Dispersion and chromaticity are effects caused by a particle being off-momentum compared to the design momentum, p_0. These effects will only be described qualitatively here, to make the reader acquainted with the concepts. For a more complete discussion, see [10].

The curvature of a particle's trajectory in dipoles depends linearly on the particle momentum. If a particle is off-momentum, it will have a trajectory with a curvature different from the reference particle. Hence, the betatron amplitude of a particle will depend on its momentum. This is the effect known as dispersion.

In a quadrupole, the trajectory of charged particles is focused towards or away from the beam axis. This is used to adjust the beam size throughout the accelerator ring. How much a particle is focused, depends on the particle momentum as well as the magnetic field strength. Chromaticity is the momentum dependence of focusing, and affects the betatron tune.

2.1.8 Beam Size and Emittance

Assuming that dispersion is negligible, the RMS beam size can be calculated as

$$\sigma_z = \sqrt{\beta_z \varepsilon_z}.$$

Here, ε_z is the RMS beam emittance, defined as

$$\begin{aligned}
\varepsilon_z &= \sqrt{\sigma_z^2 \sigma_{z'}^2 - \sigma_{zz'}^2}, \text{ with} \\
\sigma_z^2 &= \langle z^2 - \langle z \rangle^2 \rangle, \\
\sigma_z'^2 &= \langle z'^2 - \langle z' \rangle^2 \rangle, \text{ and} \\
\sigma_{zz'}^2 &= \langle (z - \langle z \rangle)(z' - \langle z' \rangle) \rangle.
\end{aligned}$$

In these equations, $\langle z \rangle$ defines the expectation value of z, for a particle distribution function $\rho(z, z')$.

From all this, we see that the beta function and the beam emittance together define an envelope function for betatron oscillations. The beam emittance is a global property of the beam, and is (in the linear approximation) a conserved quantity. The beta function, on the other hand, depends on the optics of the machine, and is a local quantity. Note that the beam size can be very different in the horizontal and vertical plane, especially for electron machines.

2.1.9 Betatron Tune and the Working Diagram

We define the (global) betatron tune as

$$Q_z = \frac{\mu_z}{2\pi} = \frac{1}{2\pi} \int_0^L \frac{\mathrm{d}s}{\beta_z(s)}.$$

The tune is equal to the number of betatron oscillations per turn in the ring. The tune is an important concept for ring accelerators, as the stability of betatron motion depends heavily on the tune. Also, the tune of the SPS affects the speed of which the scrapers remove protons from the beam tails.

In general, if the fractional tunes ν_x, ν_y satisfy the relation

$$l\nu_x + m\nu_y = p, \tag{2.16}$$

with l, m, p integer, one has a resonance of order $|l| + |m|$. If this condition is fulfilled, magnet errors will add up for each turn in the ring, giving the particle growing betatron

amplitude. To avoid this, it is essential that the tune is selected carefully, and is as far as possible from any resonance condition. Lines satisfying Equation (2.16) up to $p = 3$ and $p = 5$ are plotted in Figure 2.2. In proton storage rings with a long lifetime, one has to consider resonances of more than 10th order when designing the optics.

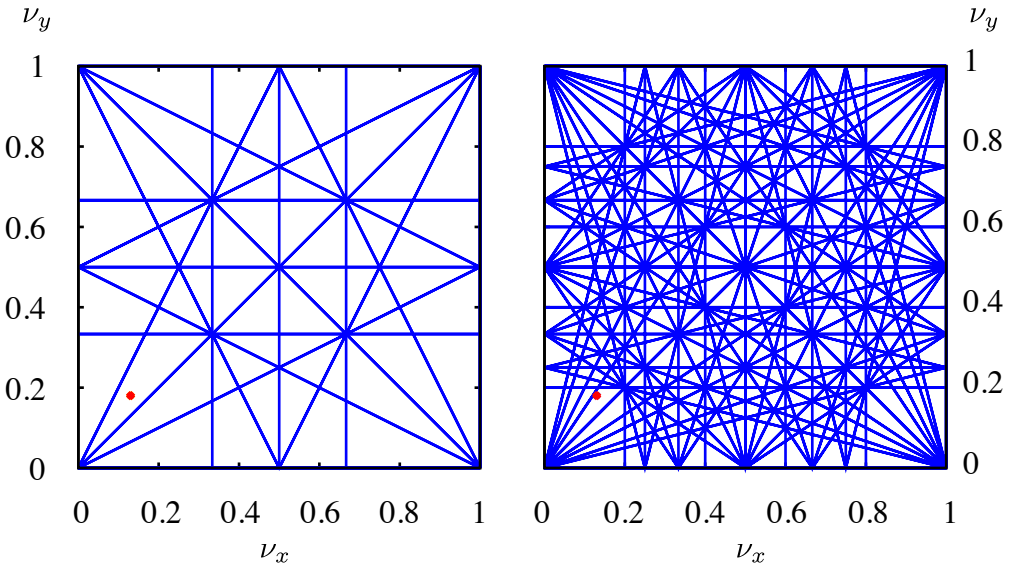

Figure 2.2: Working diagrams showing optics resonances up to 3rd and 5th order. The SPS working point is marked with a red spot.

2.1.10 Amount of Beam Scraped

To get an estimate of how much of the beam is scraped, let us assume a standard Gaussian particle density (i.e. $\mu = 0$, $\sigma = 1$) in 2-dimensional normalized phase space (x, x') given by

$$\rho(x, x') = \frac{N_0}{2\pi} \exp\left(-\frac{x^2 + x'^2}{2}\right).$$

N_0 is the number of particles in the beam. Let us also assume the scrapers to be black, in the sense that they absorb all impinging protons immediately.

To calculate the fractional intensity reduction due to scraping, N_s, one calculates the integral [12]

$$N_s(x_s) = \int_{-\infty}^{\infty} \mathrm{d}x \int_{-\sqrt{x_s^2 - x^2}}^{\sqrt{x_s^2 - x^2}} \mathrm{d}x' \rho(x, x').$$

This is equivalent to an elliptical cut in phase space, caused by the beam's rotation in phase space as given by the single turn matrix. For normalized phase space coordinates, the linear transfer matrix becomes a pure rotation matrix.

Using this formalism, and assuming a Gaussian beam distribution, Table 2.1 and Figure 2.3 have been constructed. They show the amount of beam scraped for different

Table 2.1: Fraction of particles in the beam removed by scraping

x_s/σ_x	N_s/N_0
0.5	0.88
1.0	0.61
1.5	0.33
2.0	0.14
2.5	0.044
3.0	0.011
3.5	0.0022
4.0	0.00034

scraping positions. Note especially the low amount scraped at the nominal scraping position, 3.5 σ, for Gaussian distributions. A significant deviation from this low number could be an indication of poor beam quality.

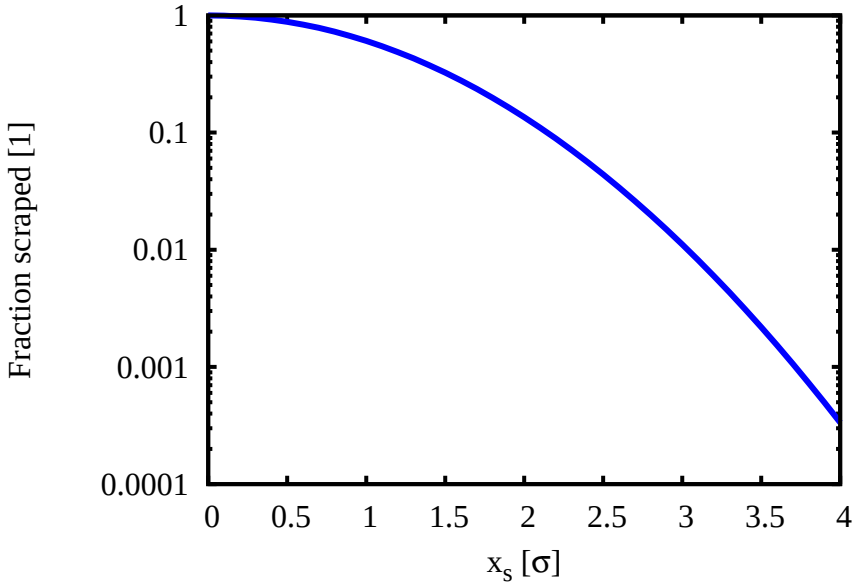

Figure 2.3: Fraction scraped as a function of the scraping position x_s.

2.2 Longitudinal Particle Motion

In order to earn the name "accelerators", particle accelerators utilize longitudinal electrical fields to accelerate charged particles. Modern day synchrotrons use so-called RF cavities to accomplish this. Here, as opposed to in early electrostatic accelerators, a time varying longitudinal electrical field is used to accelerate the particles. We will not

delve deeply into the details here, but instead use a simple model to understand the basic dynamics and stability of the longitudinal oscillations of accelerated particles.

2.2.1 Discrete Kick Model of Longitudinal Motion

To a good approximation, the longitudinal motion of particles can be modeled as a series of discrete longitudinal kicks. The motion has two degrees of freedom: the longitudinal particle momentum, p_s, and the longitudinal particle position, s. Particle momentum is usually described in terms of fractional off momentum, δ, defined as

$$\delta = \frac{p_s - p_0}{p_0}.$$

p_0 is here the design momentum of the accelerator. The longitudinal particle position can be mapped to its RF phase relative to that of the synchronous particle, ϕ. The synchronous particle is the particle which does not oscillate in longitudinal phase space from turn to turn. In other words, it is synchronous with the accelerating RF fields.

The nonlinear kick model is then the following:

$$\begin{aligned}\delta_{n+1} &= \delta_n + \frac{eV}{\beta^2 E}\left(\sin\phi_n - \sin\phi_s\right), \\ \phi_{n+1} &= \phi_n + 2\pi h\eta(\delta_{n+1})\delta_{n+1}.\end{aligned}$$

Here, ϕ_s is the RF phase angle (which can be changed to accelerate or decelerate the particles), e is the electron charge, V is the RF voltage, E is the particle energy, and β is the relativistic $\beta = v/c$. For an energy plateau, where there is no acceleration, we have $\phi_s = 0$. $\eta(\delta)$ is the phase-slip function

$$\eta(\delta) = \alpha_c - \frac{1}{\gamma^2}.$$

η basically states the effect of a particle being off momentum on the particle's revolution frequency compared to that of the synchronous particle. Note that η can be both greater than or less than 0, meaning that a higher energy particle can in fact have a lower revolution frequency than a lower energy particle. The relativistic Lorentz γ can be expressed as

$$\gamma = \gamma_0\sqrt{1 + 2\beta_0^2\delta + \beta_0^2\delta^2}$$

where the subscript 0 denotes the value of the synchronous particle. Note that β and γ here are the relativistic, and not the Courant–Snyder, parameters. Intuitively, this model can be thought of as a "kick" changing the particle's momentum, followed by a drift to the next cavity. During the drift, the particle's phase changes because the particle is not at the design momentum.

2.2.2 Synchrotron Tune

Analogous to the betatron tune, we define the linear synchrotron tune, Q_s, as the number of synchrotron oscillations per turn in the ring for a particle with a small, but nonzero value for δ. The value of Q_s can be calculated from the following formula, derived from the longitudinal equations of motion [10]:

$$Q_s = \sqrt{\frac{heV|\eta_0 \cos\phi_s|}{2\pi\beta_0^2 E}}. \tag{2.17}$$

Here, $h = \omega_{\mathrm{RF}}/\omega_s$, the harmonic number. Typically the synchrotron tune is on the order of 10^{-3} for proton machines, which is very small compared to the betatron tune. For the SPS, using beam parameters from Table 2.2 and Table 3.1, we find that $Q_s = 4.7 \cdot 10^{-3}$ for $\phi_s = 0$, which is the case if the beam energy is kept constant (no acceleration). This is the most interesting case for the current discussion, as beam scraping is nominally performed at the top energy plateau.

Table 2.2: RF properties of the SPS

α_c	L	h	V_{RF}	f_{RF}	γ_{TR}
[1]	[m]	[1]	[MV]	[MHz]	[1]
1.919×10^{-2}	6912	4620	7.0	200	22.8

2.2.3 Longitudinal Phase Space

For $\phi_s = 0$, the longitudinal particle motion is equivalent to the motion of a pendulum. We only consider this case, as the beam is not accelerated during scraping. It is undesirable to scrape during the energy ramp, as the beam size will shrink during the ramp. There may also be some tail generation during the ramp, and it is exactly the tails one wants to remove with scraping.

The enclosed area of phase space in which particles stay indefinitely, is known as the RF "bucket". The outermost closed trajectory in Figure 2.4 is essentially on the bucket limit. A small amplitude linear regime oscillation is shown at the center of the bucket, and a large amplitude nonlinear oscillation is shown just inside the bucket limit. Also, a particle outside the RF bucket is shown.

The particles contained inside a bucket are called a bunch of particles. An important parameter for an accelerator is the RF or momentum acceptance, which is the half height of the RF bucket in phase space. This value tells us how much off momentum a particle can be before it loses longitudinal stability.

The following formula gives the momentum (or RF) acceptance [13]:

$$\Delta\delta = \pm\beta\sqrt{2\frac{eV_{RF}}{\pi\eta_0 h p_0}}. \tag{2.18}$$

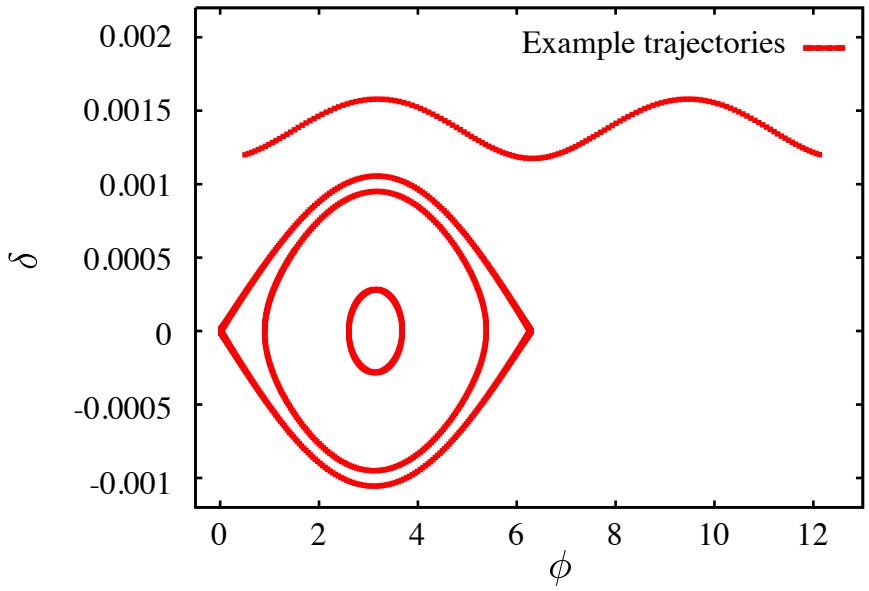

Figure 2.4: Example trajectories in the longitudinal phase plane. Four different cases are shown.

With the SPS beam parameters, the momentum acceptance becomes $\Delta\delta = 1.06 \cdot 10^{-3}$. In terms of momentum (or, to a very good approximation, energy), this becomes $\Delta E \approx c\Delta p = 0.48\,\text{GeV}$. In other words, the momentum acceptance is about one order of magnitude larger than the average loss of momentum for a 450 GeV proton passing through 30 mm of copper. This means that the momentum loss caused by the scraper is not going to be the main mechanism for removing protons from the beam.

3 Robustness of Scrapers and Aperture Elements

In this chapter, the robustness of the scraper and aperture elements downstream from the scraper is discussed. A quick estimate shows that the beam energy is more than large enough to melt the scrapers (see Chapter 1.6.4). More detailed computer simulations of beam losses and the beam's interaction with the scraper jaw show that care must be taken to avoid damage to the scrapers.

3.1 Experimental Results on Materials Damage from Beams

In a paper by Kain et al. [14], an experiment on material damage by beam impact is described. An SPS beam with a beam energy of 450 GeV and an intensity of $7.9 \cdot 10^{12}$ protons (about 25% of nominal LHC injection intensity) was directed onto a metal target. Beam sizes were $\sigma_x = 1.1$ mm and $\sigma_y = 0.6$ mm. The target consisted of a number of 2 mm thick metal plates with air spacing between them. One third of the metal plates were copper, one third stainless steel, and one third zinc. The beam melted copper after passing through 72 mm of metal.

The scraper jaws have an active length of only 30 mm. They are placed in an area with a smaller beam size, $\sigma_x = 0.62$ mm and $\sigma_y = 0.58$ mm. Beam intensity will also be higher ($3.3 \cdot 10^{13}$) during nominal LHC injection. In addition, the movement of the jaws will concentrate heat deposit from the beam on the jaw surface. We thus expect melting of the scraper jaws to occur if a large fraction of the beam is scraped.

3.2 Spatial Beam Loss Distributions

It is interesting to know to which degree scraped protons are absorbed in the scraper jaws themselves, as opposed to being scattered in the scrapers and absorbed in downstream collimators or aperture. Both simulations and machine studies have been performed to investigate this. Simulations have been performed with SixTrack, a particle tracking code used at CERN. Machine studies have been performed with collimators at different settings to measure loss distributions around the SPS ring.

3.2.1 Experimental Beam Loss Distributions

Spatial beam loss distributions have been measured during several Machine Development (MD) sessions. Measurements have been done with collimators at several different positions when scraping. It has been shown that collimators are able to absorb a large fraction of scraped protons. To achieve this, the collimators have to be moved closer to the beam than allowed by beam injection. This is only possible to do for coasting beams (beams kept at constant energy, but kept bunched with RF cavities). Figure 3.1 shows a spatial beam loss measurement done with primary and secondary vertical collimators in at ±7 mm, and horizontal collimators out. Injection requires a vertical half aperture of 20.9 mm at the primary collimators and 21.1 mm at the secondary collimators. [4]. Even when collimating significantly closer to the beam than injection allows, the strongest signal comes from the BLM directly behind the scrapers, before the collimators.

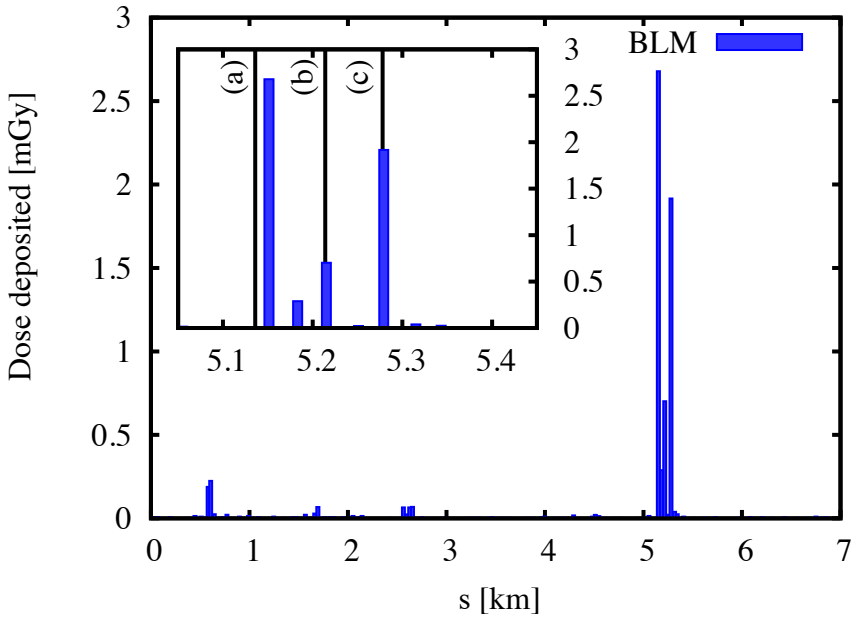

Figure 3.1: Experimental spatial beam loss measurement from November 15, 2006. During this measurement, scraping (a) was conducted with vertical primary (b) and secondary (c) collimators set at ±7 mm, and horizontal collimators out.

Figure 3.2 shows a spatial beam loss measurement made with collimators out. Beam losses are spread more around the ring in this case. The BLMs closest to the scrapers are saturated. A loss map with collimators at injection compatible settings is shown in [2]. This loss map is essentially identical to Figure 3.2. Hence, collimators at injection compatible settings have a negligible effect on the spatial distribution of beam losses.

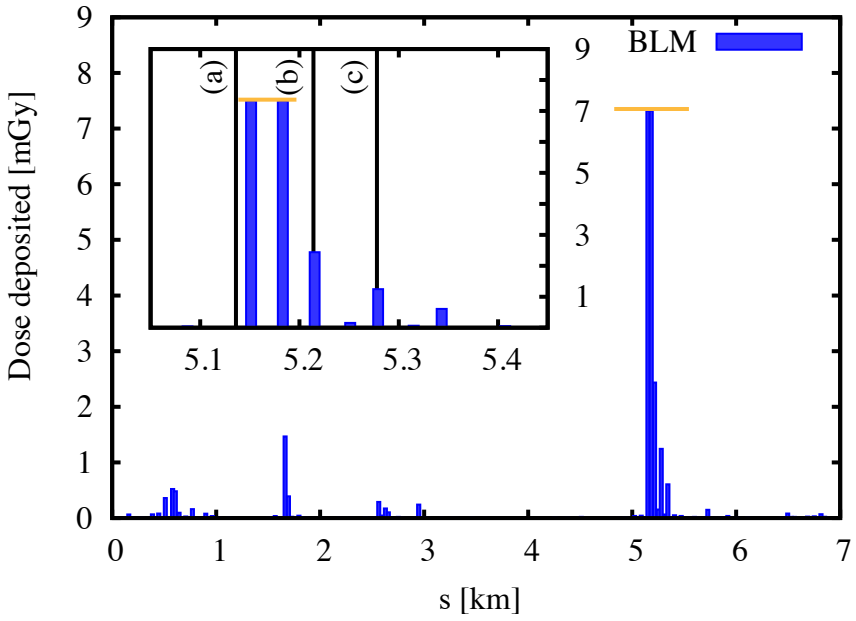

Figure 3.2: Experimental spatial beam loss measurement from September 12, 2007. Scrapers are marked by vertical line (a). Collimators, marked by vertical lines (b) and (c), were out during this measurement. The yellow line marks the BLM saturation limit.

3.2.2 SixTrack Beam Loss Simulations

To understand the spatial loss distributions, SixTrack tracking and collimation simulations have been performed. Halo protons are tracked throughout the SPS ring and the position of absorption is calculated. Ionization and scattering interactions is simulated for the scrapers and collimators, to determine where scraped protons end up. If the proton hits any other aperture restriction, the proton is assumed to be lost immediately. Figure 3.3 shows that the scraper jaws absorb over 80% of the scraped protons. Collimators absorb about 10% of the scraped protons and other aperture limitations absorb about 10% as well. In this simulation, beam parameters for top energy were used. Collimators were set at injection compatible settings.

The correspondence between simulations and experiments is reasonably good. Qualitatively, the plots look similar. Unfortunately, it is difficult to calculate dose rates in the beam loss monitors from a loss map like Figure 3.3. Measured dose rates are affected by the position of the loss monitors relative to the collimators and scrapers. Measurements and simulations both indicate that one can, to a good approximation, neglect collimator and aperture absorption of scraped particles in simulations of scraper-beam interaction.

3.2.3 Efficiency of Collimators During Scraping

As has been shown here and by others [2], the downstream collimators associated with the scrapers have limited usability under the current scheme for LHC injection. Due

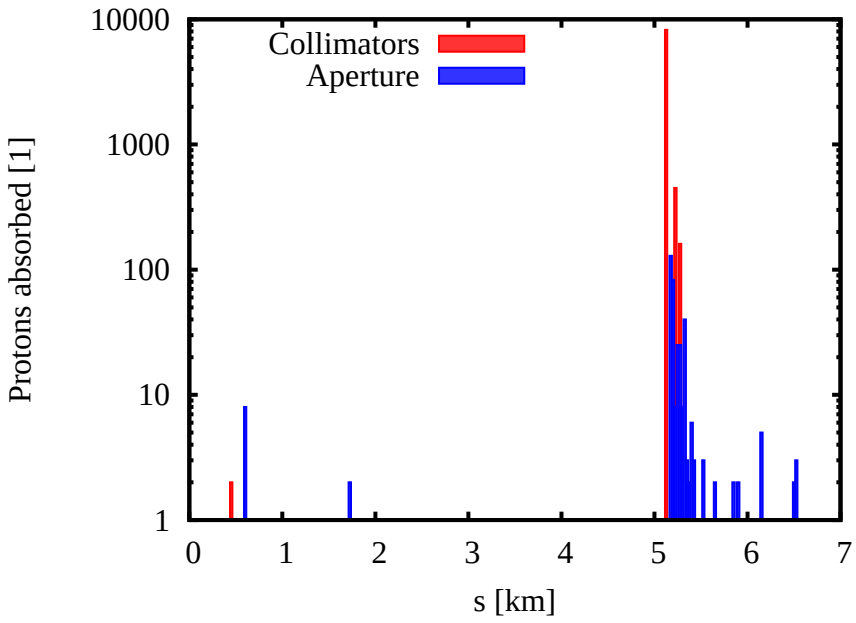

Figure 3.3: Simulated beam loss distribution from SixTrack with aperture impact detection. Note the sharp loss peak at the scrapers. Collimators were set at injection compatible settings.

to aperture requirements, the collimators are forced to stay far from the beam axis during injection. Because the beam shrinks during the energy ramp, the collimators are inefficient at top energy when set to injection compatible settings. As the collimator movement is slow, the energy ramp of a few seconds is too short to move them in.

While working with coasting beams, collimators can be adjusted closer to the beam center, allowing them to intercept scraped protons and avoid scraping induced beam losses around the rest of the ring. This suggests that collimators moving in during the energy ramp would help keep losses local. Pulsed collimators would have to move relatively quickly, as the energy ramp is only a few seconds long. As most losses occur close to the scraper even without collimators, the gains of doing this may not be worth the effort.

3.3 Simulations of Scraper Jaw Energy Deposition

Simulations of interactions between the beam and the scraper jaw have been performed using the Geant4 toolkit [15, 16]. This has been done to calculate energy deposition profiles for different scenarios, and to estimate the effects of the beam impact on the scraper jaw. Geant4 is a C++ toolkit for simulating the passage of particles through matter. It is used by space agencies, medical research institutions and the high energy physics community to simulate particles interacting with detectors, human tissue, electronics,

and other materials.

Simulations were used to analyze scraping time dependence and hardware robustness. Building on the fact that the scrapers intercept and absorb the majority of scraped protons (see Chapter 3.2), losses in aperture and collimators have been neglected in these simulations. Particle tracking has been performed using a one-turn map approach.

Parameters for the simulated beam were calculated using MAD-X. The beam parameters are shown in Table 3.1 and Table 3.2. The initial beam distribution was generated to match these parameters. To generate the proton distribution in six dimensional phase space, a Gaussian distribution in normalized coordinates was generated for each dimension. The real space distribution was then created by transforming the distribution in normalized coordinates. For some simulations, a "donut" distribution (not including protons with betatron amplitude smaller than x_s) was used to decrease the required computing time.

Table 3.1: Global parameters for LHC injection beam in the SPS

Parameter	$\varepsilon_x, \varepsilon_y$	σ_δ	$c\sigma_t$	p	Q_x	Q_y
Unit	[µm]	[10^{-3}]	[m]	[GeV/c]	[1]	[1]
Value	3.5	0.287	0.129	450	26.13	26.18

Table 3.2: Local parameters at scrapers for LHC injection beam in the SPS

Parameter	β_x	β_y	σ_x	σ_y	α_x	α_y
Unit	[m]	[m]	[mm]	[mm]	[1]	[1]
Value	52.5	46.5	0.62	0.58	1.49	-1.36

3.3.1 Full Beam Impact on Static Piece of Copper

To gain some intuition about energy deposition density, a full beam impact on a static piece of copper was simulated. Beam size and momentum was set to $\sigma_x = \sigma_y = 0.60$ mm and $p = 450$ GeV/c. The thickness of the copper piece was set to 30 mm, the same as for the scraper jaws. This setup is similar to the experiment conducted in [14], which should give some indication of whether the simulation results are correct or not. Statistical analysis of the particle-copper interactions was also done, to compare simulations to analytical results in Chapter 1.6. As the real scraper jaws sweep quickly through the beam, this scenario is not directly comparable to any realistic cases of beam scraping.

In Figure 3.4, one can see the simulated energy deposit profile inside the copper piece. The energy deposit profile is calculated from 10^6 simulated proton impacts. Statistical analysis shows that 18% of protons underwent nuclear interactions, which is the same

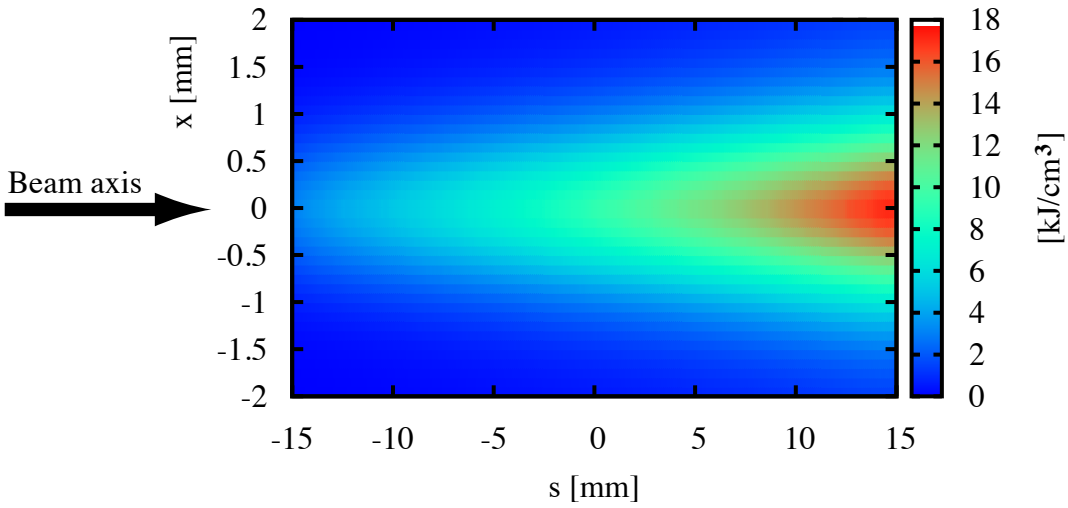

Figure 3.4: Energy deposition profile caused by a full SPS beam impact on a static piece of copper.

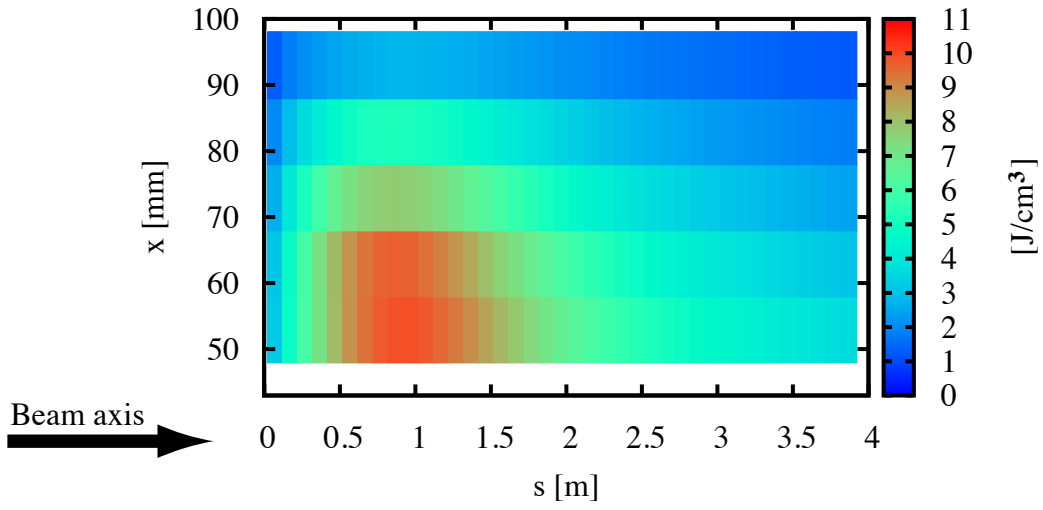

Figure 3.5: Energy deposition profile in quadrupole QD.51710, zoomed in to show the "hottest spot". The position of the beam axis is indicated (not to scale).

result as in Chapter 1.6.2. Average energy loss for protons that "survived" the passage through the copper was also found to match the analytical estimate for ionization losses, within statistical errors. As seen from the figure, the maximal energy deposition is reached at the end of the copper piece. The highest energy deposition is found to be about 18 kJ/cm^3. This energy deposit is significantly larger than the energy needed to melt copper, which is 5.5 kJ/cm^3 if the initial temperature of the copper is 300 K. The latent heat of melting is roughly 25% of this. More specifically, it takes 3.65 kJ/cm^3 of energy to heat copper to just beneath the melting point at 1358 K, when starting from 300 K. The figure indicates that the beam will cause melting after traversing about 10 mm of solid copper. Melting will occur in a very small part of the copper piece.

A control simulation of the static beam impact was performed using the FLUKA code.[1] The results were found to be in good agreement with the Geant4 simulation results. Maximal energy deposition per volume was found to be equal within statistical errors, and the energy deposition plots look qualitatively the same. This control simulation gives more confidence in the Geant4 simulation results.

Damage to Downstream Aperture Elements

A large number of secondary particles are generated by beam scraping. An important issue is whether this particle shower may damage lattice elements downstream of the scraper. A simulation of absorption of secondary particles from the scrapers in downstream elements has been performed. This simulation includes the beam pipe, two beam pipe flanges, and a quadrupole magnet, in addition to the scraper jaw. All elements were approximated as blocks of solid iron. Figure 3.5 shows the volume of quadrupole QD.51710 (MAD-X naming convention) with the highest energy deposition density. The highest energy density here is a factor 10^3 lower than the case for the scraper jaw. This is because the particle shower is spread across a large volume. Hence, elements downstream from the scrapers should not be damaged due to beam losses caused by scraping.

3.3.2 Accident Scenario: Moving Jaw Intercepts Full Beam

To investigate potential damage of the real scraper jaws, a Monte Carlo simulation with simple particle tracking was performed. A particle distribution was generated according to beam parameters found in Table 3.1 and Table 3.2, which correspond to LHC injection beam parameters. For the transverse plane, single turn matrix tracking was used. Linear optics was assumed as scraping only takes on the order of $10 - 100$ ms. For the longitudinal plane, a non-linear kick model was used [10]. Absorption of protons by collimators and aperture was neglected as these absorb less than 20% of scraped protons. Interactions between the scraper jaw and the beam protons were simulated using the Geant4 toolkit and the QGSP physics simulation engine. The scraper jaw was moved incrementally once per SPS turn during the simulation to simulate its sweep through the beam. Figure 3.6 gives an impression of the three dimensional distribution of energy deposited from the scraping.

[1] The simulation was done by R. Bruce and the data analysis by myself.

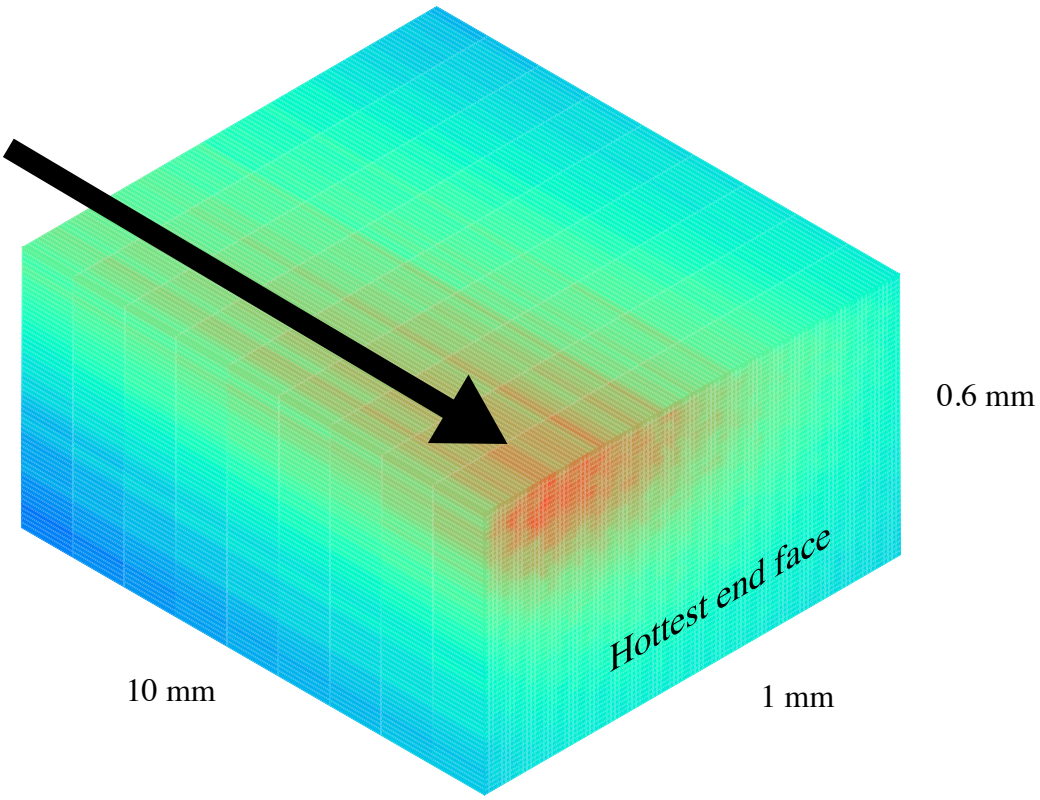

Figure 3.6: 3D model of energy deposit in moving scraper jaw. The arrow indicates the beam axis and direction. We see that the hottest end face is the one furthest from the point of impact. On the left face of the jaw, we see the build-up of a particle shower as energy deposit density increases along the beam axis. On the top of the scraper, we see that ionization loss on the edge of the jaw gives the peak energy deposit. Data for this figure were taken from the simulation described in Chapter 3.3.5.

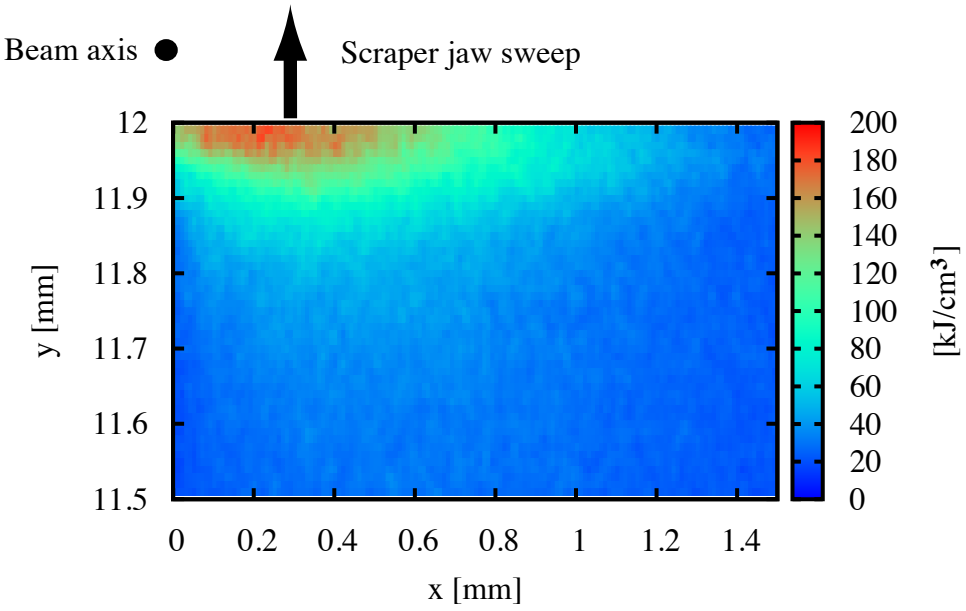

Figure 3.7: Energy deposit in the current scraper jaw when scraping the whole SPS beam. Here we see the end face with the highest energy density. The beam axis (perpendicular to the plane) and the sweep direction of the jaw is indicated.

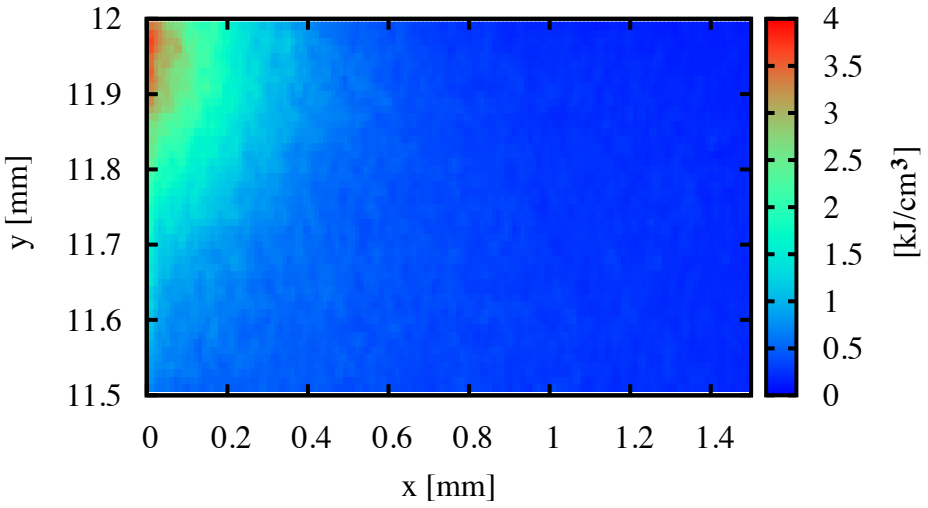

Figure 3.8: Energy deposit for scraping at 3 σ. The energy deposit density is high enough to heat the scraper jaw surface to melting temperature (1358 K), when scraping at nominal intensity.

A plot of the energy deposit density in the scraper jaw is shown in Figure 3.7. The plot shows the end face of the jaw which is perpendicular to the beam. The simulated beam has its center at $x = 0$ in this plot. In the jaw's upper left corner, one observes a large peak of energy deposition. Compared to the static impact scenario (Figure 3.4), the beam energy is spread across a volume more than 10 times smaller, and the energy deposition density is correspondingly high. In this calculation, beam intensity was set to the nominal $3.3 \cdot 10^{13}$ protons. To heat copper from room temperature to its melting point requires an energy deposit per volume of $3.65\,\mathrm{kJ/cm^3}$. Comparing this to Figure 3.7, which represents the heating from a beam with nominal LHC injection intensity, we find that beam scraping is safe if the total beam intensity is less than 1.8% of nominal intensity.

3.3.3 Nominal Beam Scraping

A simulation for beam scraping at 3 σ (close to the nominal value of 3.5 σ) has also been performed. At this setting, the scrapers should remove about 1.1% of the beam's intensity if the beam distribution is Gaussian. The result of the simulation is shown in Figure 3.8. The energy deposit density per scraped proton is almost a factor of 2 higher than is the case for a full beam impact. Even when scraping at 3 σ, the copper in the jaw is heated to melting temperature, 1358 K. If the beam tails happen to be non-Gaussian, a small part of the jaw may melt.

3.3.4 Possible Upgrade: Graphite Jaws

To make the scrapers more robust, several upgrade options have been suggested. One is to replace the current scraper jaws with similar graphite jaws. The argument is that graphite has a higher melting point than copper, and a longer interaction length. However, graphite has a lower heat capacity and lower heat conductivity. Also, as the main mechanism for removing protons from the beam is nuclear interaction, the protons will simply make a larger number of turns if the jaws are made of graphite.

In Figure 3.9, simulation results for a graphite jaw with an active length of 30 mm is shown. The energy deposit is spread out somewhat compared to the copper case. Given a maximum energy deposit of $60\,\mathrm{kJ/cm^3}$, the safe beam intensity is about $3.1 \cdot 10^{12}$ protons. At this intensity, the graphite will start sublimating. This is not a desirable property in accelerators where vacuum quality is very important. It is clear that substituting copper for graphite is not a "miracle" solution to the hardware protection problem.

3.3.5 Possible Upgrade: Thinner and Faster Scraper Jaws

A different approach would be to make new copper jaws that are thinner and faster. Simulations have been done for a copper jaw with 10 mm active length and 2 m/s sweep speed. Decreased active length and increased sweep speed both help spread the energy deposit across a larger volume.

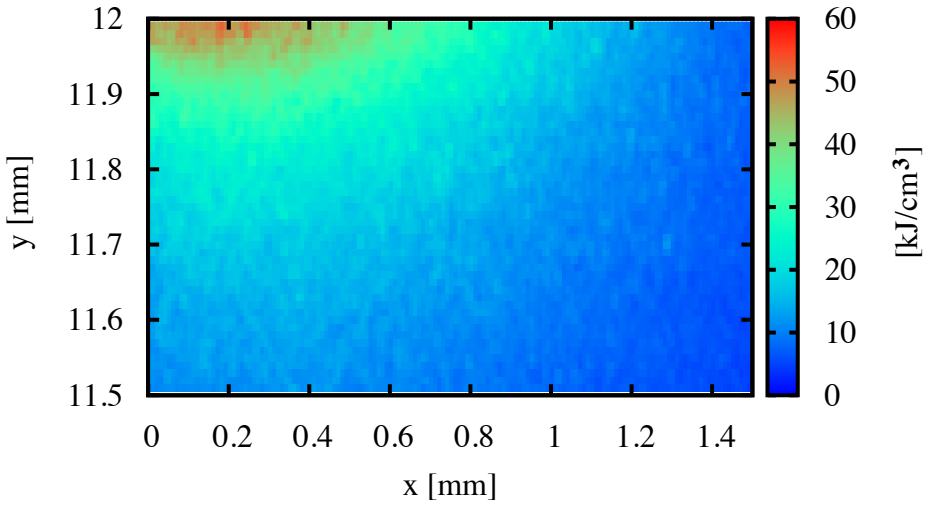

Figure 3.9: Energy deposit in a simulated graphite scraper jaw, intercepting the full SPS beam.

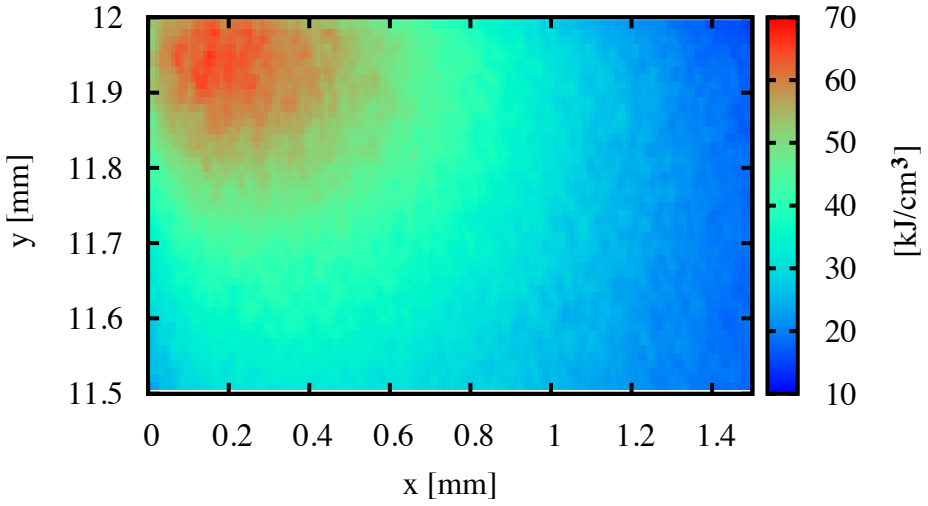

Figure 3.10: Energy deposit density for faster and thinner scraper jaws. In this simulation, the jaws have an active length of 10 mm. The sweep speed has been set to 2 m/s.

Simulation results are shown in Figure 3.10. A significantly lower energy deposit density indicates that this is an interesting approach. A thinner jaw means that less of the secondary particle shower is caught inside the jaw. This seems like a more promising approach than graphite jaws: the maximum energy deposit density is found to be about 66 kJ/cm^3, a factor 3 less than the current system. This would improve the robustness of the scraper system noticeably. Simulations also show that a 10 mm scraper jaw is more than thick enough to remove all halo particles from the beam. Even thinner jaws should be investigated if one is to design a new scraper system.

3.3.6 Mechanical consequences of scraper jaw heating

Only the deposition of heat due to scraping has been calculated so far. To get a complete understanding of how heat deposit affects the jaws, one would ideally put the simulated three dimensional heat deposit histograms into a computer model to calculate heat transfer and mechanical effects. This has already been done extensively for the LHC collimators, and the same should be possible to do for the scrapers. The two most important questions to answer are the following: will heat conduction be able to remove the heat efficiently when scraping repeatedly every user cycle for LHC injection? Can the scraper jaw be deformed by heat expansion? These questions have not been answered, but are important for regular operations.

3.4 Summary of Robustness Considerations

Numerous simulations and estimates show that scrapers may be damaged when scraping high intensity beams. Even the nominal scraping at 3.5 σ foreseen in [4] could melt the scrapers if non-Gaussian tails are present. Scraping of high intensity beams should not be performed until a better hardware protection system, such as a fast beam interlock, is in place.

By replacing the scraper jaw material by graphite, the energy deposit density drops somewhat. Graphite, however, has a lower heat capacity and sublimates when heated. Because of this, graphite is not necessarily a good material for fast scrapers.

A combination of increasing the sweep speed of the jaws and making the jaws thinner is likely a better way to reduce the heating problem. Simulations show that a thin copper jaw (10 mm active length) with a 2.0 m/s sweep speed will be efficient at removing beam tails at nominal tunes, while reducing the energy deposit density considerably.

Downstream collimators are currently unable to absorb scattered protons efficiently (see Chapter 3.2). A scheme with collimators moving in during the energy ramp could be considered, but may prove to be impractical. Also, misalignment or the collimators failing to move would endanger the scrapers. In addition to this, collimators cannot remove the heat deposit from the protons' first impact on the scraper jaw.

A beam interlock system currently exists in the SPS. The current system monitors beam losses with a 20 ms time resolution, which is less time than it takes for the scrapers to sweep through the beam. This is shown in Chapter 4.1. To avoid damage to the

scrapers, a fast beam interlock system should be installed, as foreseen in [4]. The beam interlock would dump the beam if a too large fraction of the beam intensity is scraped. This system can also be used to prevent injection of dirty beams with non-Gaussian transverse tails into the LHC, making beam quenches less likely.

4 Efficiency of Scraping

The efficiency of scraping has been both simulated and measured in machine studies. Important aspects are how quickly protons are removed from the beam, and if the beam stays clean after scraping. It is essential that the beam scrapers are able to ensure the absence of transverse beam tails when the beam is injected into the LHC.

4.1 Time Dependence of Scraping

The time dependence of beam losses from scraping has been modeled analytically, simulated, and measured. Measurement is done with the fast LHC Beam Loss Monitors (BLM), installed for testing in the SPS. Results from the three methods are compatible. An important result is that the measured time distribution of scraping can be used to estimate the beam size. Time dependent losses are also able to reveal other interesting details about the beam.

4.1.1 Theory

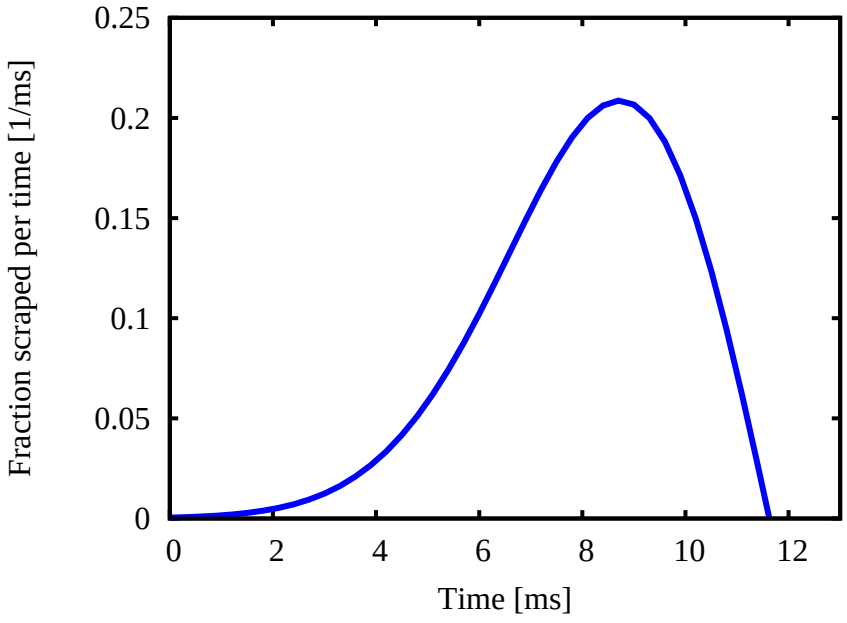

Figure 4.1: Time dependent beam loss, calculated analytically. The area under the curve is normalized to 1.

For circular accelerators, one usually assumes a Gaussian distribution function in normalized phase space for the beam:

$$\rho(z, z') = \frac{1}{2\pi} \exp\left(-\frac{z^2 + z'^2}{2}\right). \tag{4.1}$$

Here, we let z denote either x or y; the treatment of the two planes is identical. We have chosen

$$\int_{-\infty}^{\infty}\int_{-\infty}^{\infty} \rho(z, z')\,\mathrm{d}z'\,\mathrm{d}z = 1.$$

As the two planes are well decoupled in the SPS, we can assume that the distribution functions in the (x, x') and (y, y') planes are independent. Let us also make three more assumptions: that we are far from any strong tune resonances, especially integer, half integer or quarter integer resonances; that the scrapers are black, in the sense that they instantly absorb any impinging protons; and that the jaws move slowly compared to the betatron oscillation. Letting x_s be the horizontal scraping position in beam σ, y_{st} the initial vertical position of the scrapers, v_σ the jaw sweep speed measured in beam σ per second, and t the time, we have that the fraction of beam scraped as a function of time, $F_s(t)$, is

$$F_s(t) = \int_{-x_s}^{x_s} \int_{-\sqrt{x_s^2 - x^2}}^{\sqrt{x_s^2 - x^2}} \rho(x, x')\,\mathrm{d}x'\,\mathrm{d}x \int_{-y_s(t)}^{y_s(t)} \int_{-\sqrt{y_s^2(t) - y^2}}^{\sqrt{y_s^2(t) - y^2}} \rho(y, y')\,\mathrm{d}y'\,\mathrm{d}y.$$

Here we have that $y_s(t) = y_{st} - v_\sigma t$, the vertical position of the scraper as a function of time, with y_{st} being the starting position of the jaw. The BLM signal, however, is proportional to $\mathrm{d}F_s(t)/\mathrm{d}t$. For the Gaussian distribution in Equation (4.1), we have

$$\frac{\mathrm{d}F_s(t)}{\mathrm{d}t} \propto (y_{st} - v_\sigma t) \exp\left(-\frac{(y_{st} - v_\sigma t)^2}{2}\right), \quad t \in \left(0, \frac{y_{st}}{v_\sigma}\right).$$

Here, we neglect the proportionality constant; it is in any case very difficult to calculate the prefactor for a BLM signal. The prefactor can be determined by curve fitting if necessary. The shape of the beam loss rate curve is independent of the scraping position x_s. A plot of this function is shown in Figure 4.1. In this figure, parameter values are set to $\sigma_y = 0.58$ mm and $v = 20$ cm/s, which are the nominal values.

It can be shown that the time distribution of losses is related to the beam profile by an Abel transformation [17]:

$$\frac{\mathrm{d}F_s(t)}{\mathrm{d}t} \propto -t\frac{\mathrm{d}}{\mathrm{d}t}\int_t^\infty \frac{u\rho_x(u)}{\sqrt{u^2 - t^2}}\,\mathrm{d}u.$$

Here, ρ_x is the beam profile in x. By using the inverse transform, one can in principle get from the BLM signal to the beam profile. This is only possible if the BLM signal quality is good which is not always the case; see Figure 4.5 for an example. While conventional methods for measuring beam profiles are preferable over scraping, the scrapers in combination with BLMs allow the detection of very low intensity beam tails.

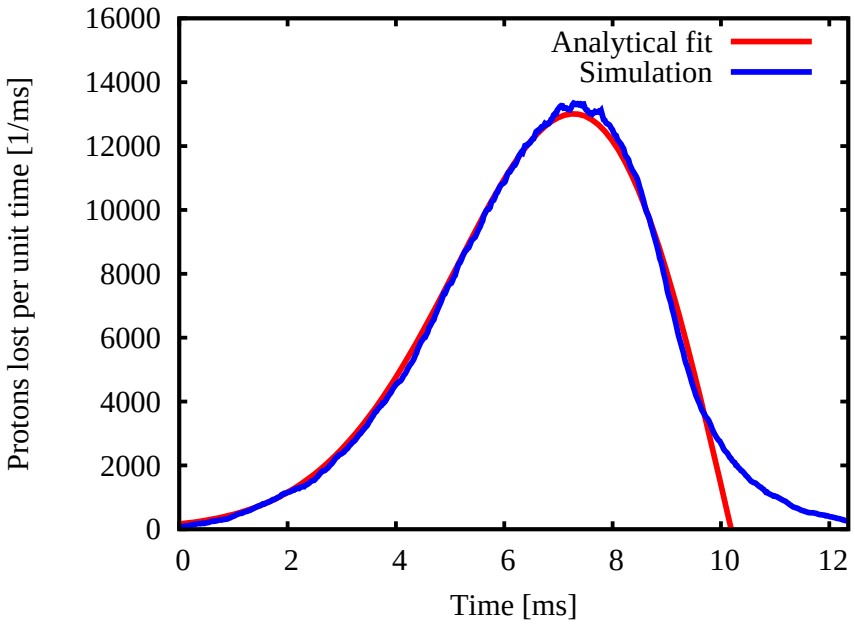

Figure 4.2: Simulated time dependent beam loss pattern. By fitting the height of the curves, the analytical model fits well to the simulation result. A beam halo consisting of 10^5 protons was simulated. The blue curve has been smoothed as turn to turn statistical variation is large.

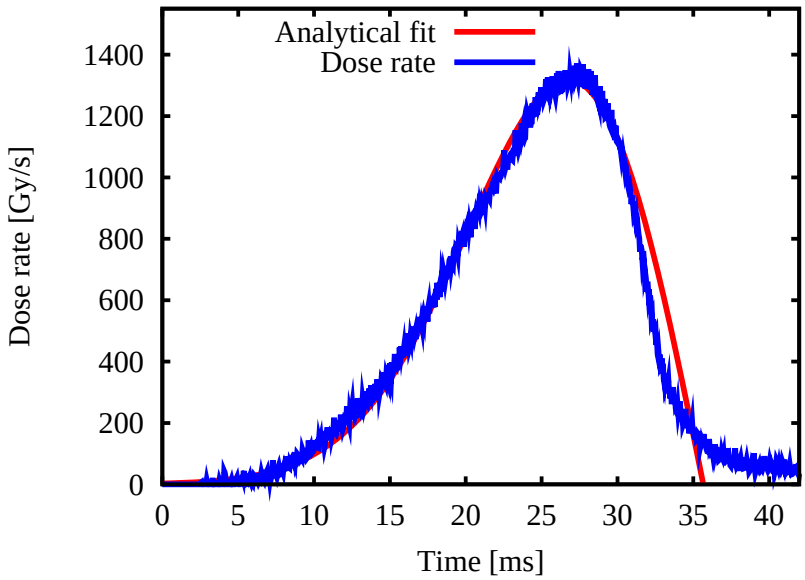

Figure 4.3: Time dependent beam loss from MD on September 25, 2007. The signal was recorded during vertical scraping. A fit of the analytical model has been obtained by fitting both y_{st}, curve height and v_σ. The latter indicates that either the beam size or the sweep speed was different from simulations.

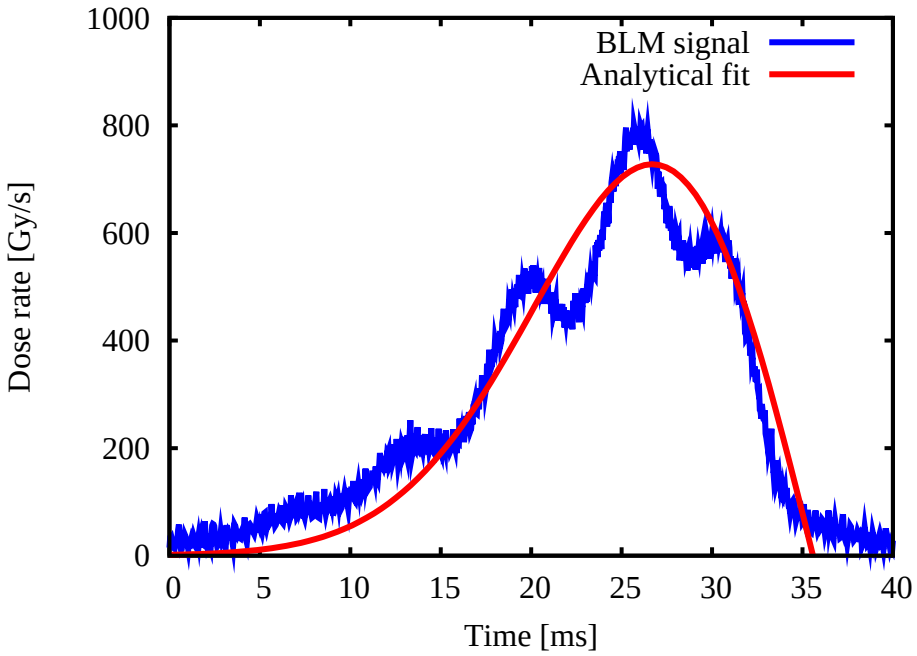

Figure 4.4: BLM measurement with oscillations. The base frequency of the oscillations is close to 150 Hz, which is the frequency of power supply ripple. Synchrotron oscillations could also cause these oscillations. For comparison, the analytical fit from Figure 4.3 is shown.

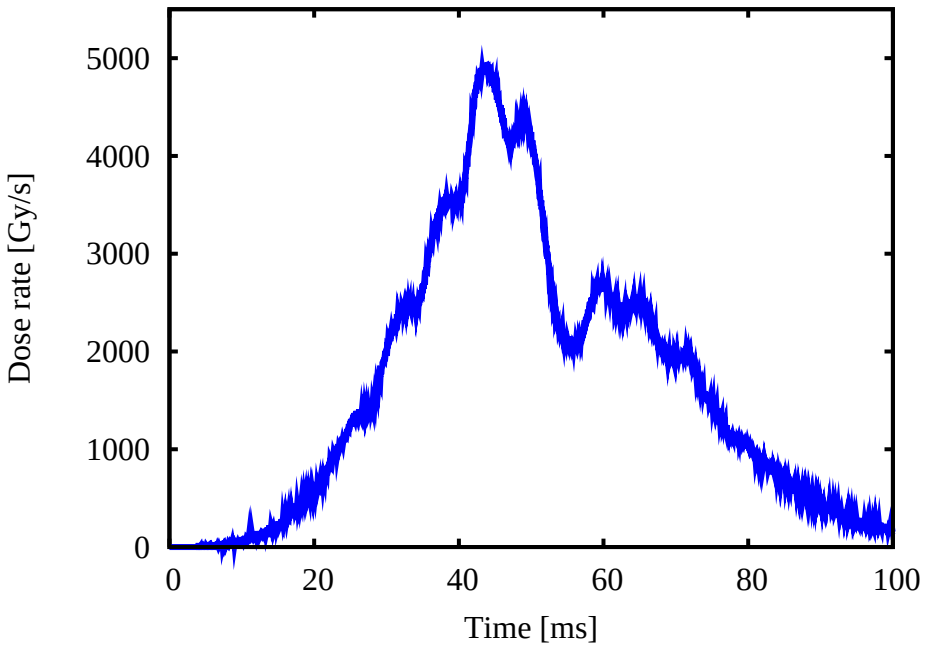

Figure 4.5: BLM measurement of vertical scraping of a poor quality beam. Scraping was performed during adjustment of beam parameters.

4.1.2 Simulations

The time dependence of beam losses was simulated together with the energy deposit, as described in Chapter 3.3. This was done by registering the number of protons lost each SPS turn. The result is shown in Figure 4.2. The nominal LHC injection beam size and a sweep speed of 20 cm/s was used. Simulating a Gaussian beam halo of 10^5 particles, while scraping at 3 σ, the result should be comparable to the nominal scraping scenario. Comparison with the analytical model shows that the time scale of scraping is close to identical, except for the "tail" at the end of the scraping. This "tail" is expected because the scrapers are not "black", as assumed in the analytical model.

4.1.3 Machine Studies

During machine studies of tail repopulation, BLM time dependent losses were recorded using an LHC BLM installed in the SPS for testing. By fitting the analytical model to the loss pattern, using a least squares error algorithm, one can see that the analytical model is good during most of the scraping. At the very end of the scraping, the real measurement diverges somewhat from the analytical model. This is as expected from simulations. By rescaling the time axis of the simulation time dependence, and superposing it on top of the measurement in Figure 4.3, one sees that measurement and simulation is compatible save for the parameter v_σ.

The time scale of the measurement is different from the time scale of the analytical model; it was necessary to fit v_σ to the measurement to obtain a good fit. This means that either the beam size, or the scraper speed, or both, were different from the values used in the analytical calculation.

BLM measurements are at times more noisy than in Figure 4.3. Several noise sources have been identified; betatron tune and power supply ripple or energy oscillations are the most apparent ones. Figure 4.4 shows oscillations with a frequency of about 150 Hz, which is compatible with the ripple of a 3-phase power supply, or possibly synchrotron oscillations. Both dipole and quadrupole modes of synchrotron oscillations have been observed in the SPS [18]. The time scale of scraping is otherwise similar to that in Figure 4.3.

Figure 4.5 shows the time dependence of scraping of a beam during adjustment of beam parameters. The long duration of the scraping shows that the beam is big, and oscillations show that the beam is not well adjusted.

4.2 Tail Repopulation

Transverse beam "tails" (or "halo") is usually defined as unwanted, high amplitude particles in an accelerator beam. In this chapter, beam tails are defined as the part of the beam removed by scraping. Often one seeks to remove beam tails by means of collimation or scraping. Common for these methods is that it is important not only to obtain a clean, good quality beam, but to preserve the beam quality as long as necessary.

It has been shown that beam scraping cleans the beam well, but some tail repopulation has been found on time scales on the order of minutes.

Previously, transverse tails and repopulation were studied in the LEP electron-positron collider [19]. Non-Gaussian tails and tail repopulation limited maximum beam intensity and caused background noise for the experiments. In the LEP, scattering processes[1] were identified as a mechanism for scattering particles to large betatron amplitudes. Understanding tail repopulation in the SPS could turn out to be useful for the running of the LHC as well.

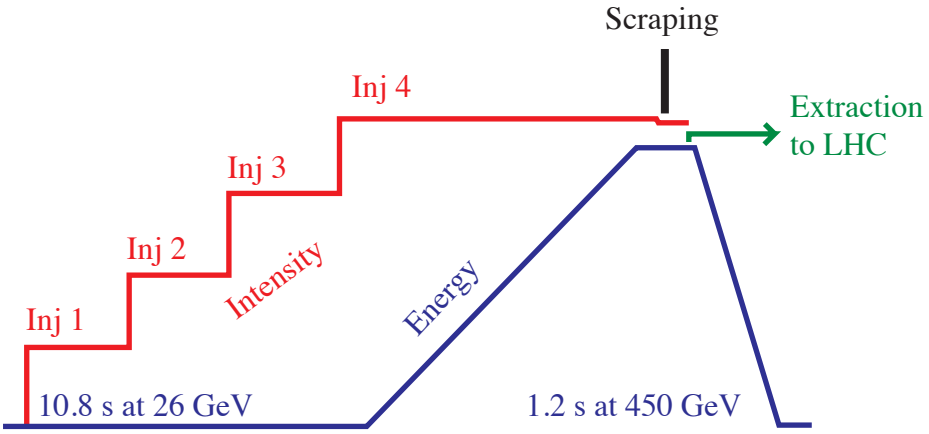

Figure 4.6: Typical SPS user cycle for LHC injection. Intensity is ramped through injection of four PS batches at 26 GeV. Afterwards, the beam energy is ramped to 450 GeV before fast extraction to the LHC takes place. Figure: H. Burkhardt.

Several different SPS user cycles have been foreseen, but they all have a short energy plateau before extraction. Figure 4.6 shows a typical SPS user cycle for LHC injection at nominal intensity. First, four batches from the Proton Synchrotron (PS) are injected. Afterwards, the energy ramp is performed. Before extraction towards the LHC, one has an energy plateau for final quality assurance of the beam. Scraping is foreseen to take place during this plateau. Machine studies have shown that the beam is kept clean for more than 1.2 s [7], meaning that tail repopulation is not an issue for LHC injection.

4.2.1 MD Measurements

Tail repopulation has been measured during several MDs, in order to determine the source(s) of tail repopulation. The main results from previous MDs have been presented in [2].

A new MD was done on September 25, 2007. Results from this MD are presented here and in [1]. A bunched beam with a constant particle momentum of 270 GeV/c

[1] Intrabeam scattering, Compton scattering on thermal photons from the beam pipe, beam-beam Bremsstrahlung, and beam-gas scattering all contribute.

was kept coasting, while it was scraped repeatedly at the same position. This allows observation of tail repopulation. Transverse dampers were shut off during the MD, but tail repopulation was observed at similar rates as previous MDs. Also, the repopulation was observed to be significantly faster in the horizontal than in the vertical plane, in agreement with previous MDs. Figure 4.7 shows scraping induced loss of beam intensity for the first coast. As we can see, horizontal repopulation takes place after a few minutes: about 60% of beam tails reappear after 5 minutes. In the vertical plane, however, little repopulation takes place even after 15 min (from $t = 700$ s to $t = 1600$ s).

A second coast was injected to get more measurement data. Results from this coast are shown in Figure 4.8. First, scraping in the vertical plane is conducted to test for repopulation. From $t \approx 450$ s, scraping was performed every super cycle to investigate repopulation on shorter time scales. After this, the scraping position was adjusted closer and closer to the beam center to see if this affected the repopulation. The figure shows that tail repopulation is faster when scraping close to the beam center.

Common for all these measurements, and for both planes, is that for nominal, high amplitude ($3.5\,\sigma$) cleaning of beam tails, the tail repopulation time is on the order of several minutes. This is much longer than 1 s, which is the requirement for nominal LHC injection.

4.2.2 Intrabeam Scattering

MD measurements of tail repopulation draw a consistent picture. On time scales on the order of minutes, there is significant tail repopulation. Assuming that beam parameters have been carefully chosen, repopulation occurs only in the horizontal plane. This indicates that an interesting physical mechanism could lie behind, and not just some noise source like power supply ripple, RF phase jitter, or similar. One has tried to remove this repopulation by turning off the RF voltage and by changing betatron tunes [2]. Neither had a significant effect on the repopulation.

A suspected source of repopulation was the transverse damper. The transverse damper is a feedback mechanism for controlling beam instabilities and kicking the beam for performing certain measurements. Transverse dampers were turned off during the MD on September 25, 2007, without any significant effect on tail repopulation.

What the dominating source of this tail repopulation is has not yet been determined. Intrabeam Scattering (IBS) is believed to be a potential source. IBS is the only hypothesis which predicts repopulation in the horizontal plane alone. IBS is a difficult mechanism to understand, but numerical packages exist to calculate the growth times. IBS is the process where many small-angle Coulomb scattering events between charged particles in a bunch increase the beam size. (A similar effect is the Touschek effect, where large-angle scattering kicks protons out from the beam entirely.) More precisely, IBS tends to increase the total six-dimensional emittance while relaxing the beam distribution in the three momentum dimensions of phase space to a spherical shape. See [20] for a discussion.

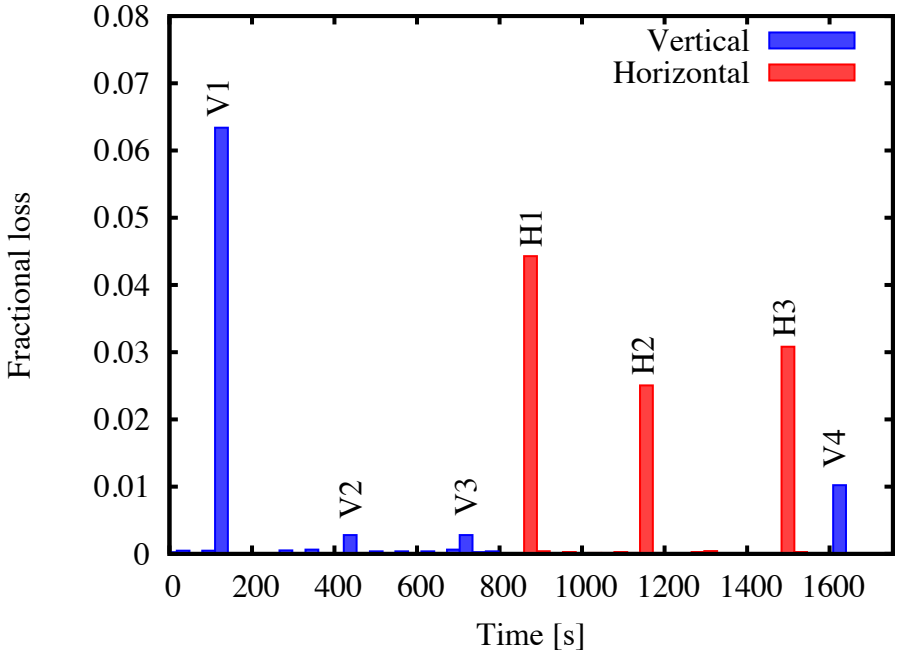

Figure 4.7: Fractional loss of beam intensity from turn to turn due to beam scraping. One bar is shown for each super cycle (approximately 31 s long).

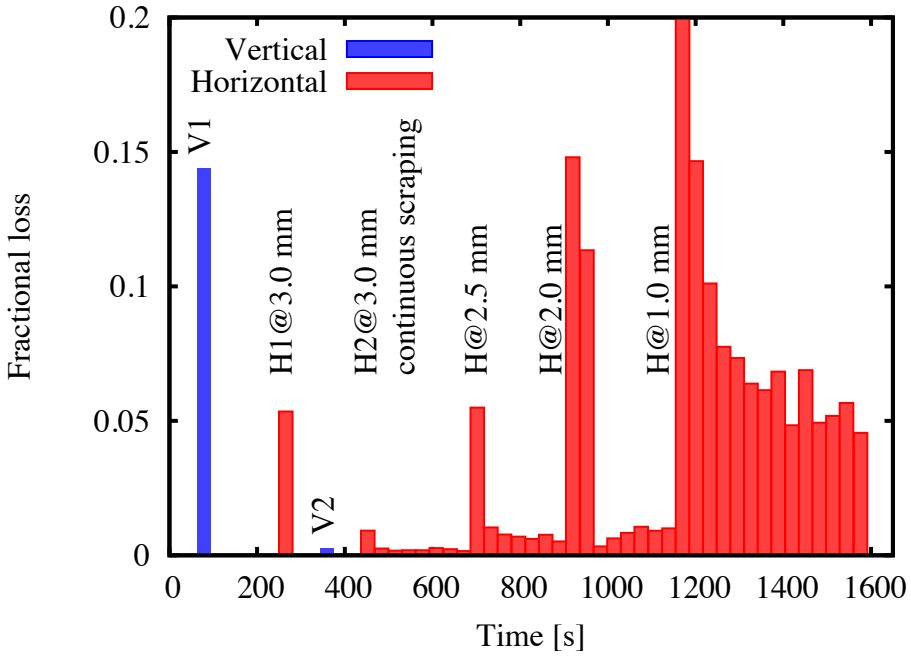

Figure 4.8: Fractional loss of beam intensity from turn to turn due to beam scraping. Note the last part where scraping is performed every cycle. The H@x_s notation denotes horizontal scraping at position x_s.

The growth rates for intrabeam scattering are defined as

$$\frac{1}{\tau_p} = \frac{1}{\sigma_p}\frac{\mathrm{d}\sigma_p}{\mathrm{d}t},$$
$$\frac{1}{\tau_x} = \frac{1}{\varepsilon_x^{1/2}}\frac{\mathrm{d}\varepsilon_x^{1/2}}{\mathrm{d}t}, \quad \text{and}$$
$$\frac{1}{\tau_y} = \frac{1}{\varepsilon_y^{1/2}}\frac{\mathrm{d}\varepsilon_y^{1/2}}{\mathrm{d}t}.$$

Here, σ_p is the longitudinal RMS beam size, τ_p is the IBS growth time in the longitudinal direction, τ_x and τ_y are transversal growth times, and ε_x and ε_y are the transversal emittances. Since the transversal beam sizes are related to the emittances by the relation $\sigma_z = \sqrt{\beta_x \varepsilon_x}$, this means that the "growth" in question is proportional to the growth in beam size.

Using the IBS module in MAD-X, these growth rates have been calculated for different beam parameters in the SPS. See Table 4.1 for an overview. Note the difference between the horizontal and vertical planes: while the horizontal plane has a growth time on the order of 10 hours, the vertical plane has a very long and negative growth time. This means that the vertical emittance shrinks as time goes by. The difference between the horizontal and the vertical plane is due to dispersion in the horizontal plane.

Table 4.1: IBS growth rates for different beam parameters in the SPS, calculated using MAD-X.

Beam	pc [GeV]	I_{bunch} [10^{10}p]	ε_x [μmrad]	ε_y [μmrad]	τ_p [s]	τ_x [s]	τ_y [s]
MD coast	270	5.0	3.5	3.5	$3.3 \cdot 10^4$	$5.1 \cdot 10^4$	$-2.0 \cdot 10^7$
High ε coast	270	5.0	7.0	7.0	$8.0 \cdot 10^4$	$2.4 \cdot 10^5$	$-9.2 \cdot 10^7$
LHC injection	26	13.0	3.0	3.0	$4.0 \cdot 10^2$	$6.6 \cdot 10^3$	$-2.1 \cdot 10^4$
LHC coast	270	13.0	3.5	3.5	$1.3 \cdot 10^4$	$1.9 \cdot 10^4$	$-7.5 \cdot 10^6$
LHC nominal	450	11.5	3.5	3.5	$3.3 \cdot 10^4$	$3.1 \cdot 10^4$	$-3.2 \cdot 10^7$
LHC ultimate	450	17.0	3.5	3.5	$2.2 \cdot 10^4$	$2.1 \cdot 10^4$	$-2.2 \cdot 10^7$

Common for all calculations are that they assume a Gaussian beam distribution in all six phase space dimensions. It should be noted that these numbers cannot readily be translated into tail repopulation time scales, as scraping leads to a non-Gaussian beam distribution with sharp edges. What we are interested in, in the case of scraping, is how quickly protons diffuse from the beam center out into the beam tails.

A suggested approach was to estimate this by looking at diffusion rate equilibrium of particles due to IBS at a given beam σ. By approximating the outwards diffusion as the only process (no scattering from the beam halo back into the "beam center"), this will give an estimate for the diffusion life time (see [21]):

$$T_x = \frac{\tau_x}{2(x_s/\sigma_x)^2} \mathrm{e}^{(x_s/\sigma_x)^2}. \tag{4.2}$$

Here, x_s is the scraping position, and T_x the life time due to diffusion processes. As an example, consider scraping at 2.5 mm in Figure 4.8. For each 31 s super cycle, about 1% of the beam diffuses into the scraped tails. This indicates a life time of about $T_x = 3.1 \cdot 10^3$ s. From the observed losses and Table 2.1, we see that 2.5 mm should correspond to about 2 σ. Equation (4.2), using the MAD-X growth time for LHC coast beam parameters in Table 4.1, gives $1.3 \cdot 10^5$ s for the life time, more than an order of magnitude longer than the measurement. This calculation indicates that IBS is a contributing factor to tail repopulation, although a small one.

The exact numerical result should not be trusted, however, as the formula assumes scraping at large amplitudes. Another significant error source is the unknown size of a beam σ and the beam position at the scrapers. In order to get a more useful measurement of tail repopulation, one would ideally measure precisely the beam position, beam profile and the size of the beam σ by an independent measurement.

Other possible sources of tail repopulation include power converter ripple and mechanical vibrations in dipole magnets. Noise with a frequency compatible with power converter ripple, which has a base frequency of 150 Hz, has been observed on the time dependent BLM signal. This is observed both during horizontal and vertical scraping.

5 Summary and Outlook

Scrapers have been tested with beam, and observations have been compared with simulations. Already during initial tests, the scrapers have proven to be very useful, and revealed interesting details about the beam.

Transverse beam tails and tail repopulation have been observed in several machine studies. Repopulation was found to be much faster in the horizontal plane than in the vertical plane, which is as expected from previous machine development sessions. Several possible sources of repopulation has been tested for and eliminated, in particular the transverse feedback mechanism. The main remaining candidates include intrabeam scattering, mechanical vibrations in dipole magnets, and power supply ripple.

Several interesting beam phenomena have been revealed with time dependent BLM measurements. By comparing BLM measurements to an analytical model, it has been demonstrated that beam scraping can be used to estimate the beam size, even when scraping far from the beam center. Machine studies also showed power supply ripple when scraping in either transverse plane.

An evaluation of the current scrapers' robustness and suggested upgrades has been done. Monte Carlo simulations show that the current scraper jaws will begin melting when scraping beam intensities higher than $6 \cdot 10^{11}$ protons, which is less than 2% of the nominal SPS beam intensity for LHC injection. A proposal has been made to make a thinner, faster scraper jaw, which will spread the energy deposit and reduce the heating problem. As foreseen in previous studies, the scrapers should be complemented with a fast beam interlock. This beam interlock should protect the scrapers from damage and prevent the extraction of "dirty" beams towards the LHC.

For regular beam scraping for LHC injection, a new and improved beam scraping system is desirable. Such a system should allow regular scraping, both for beam cleaning and for beam diagnostics, while being protected from damage. Simulation results indicate that faster and thinner scraper jaws will reduce heating problems. During MDs, the need for better low level software and diagnostics has been demonstrated. Previous studies also indicate that a diagonal scraper will give some gain in aperture at LHC injection [4].

A less urgent issue is tail repopulation. While it could be interesting to understand the mechanism behind this phenomenon, it is clear that tail repopulation does not cause problems on the time scale required for clean LHC injection.

Showers of secondary particles from the scrapers may induce radioactivity in LSS5, and cause an environmental problem. A quick estimate of the radiation generated has been done in [4], but no thorough analysis of the environmental consequences has been made.

Acknowledgements

First and foremost, I would like to thank Helmut Burkhardt for being a great supervisor. While always busy, he always has time for questions and discussions.

In addition I acknowledge (in no particular order) the help and support from the following:

- Stefano Redaelli, Thomas Weiler, and Chiara Bracco for their help on collimation and tracking studies.
- Roderick Bruce for performing FLUKA simulations of beam impact on a static jaw.
- Daniel Kramer for his help on BLM data acquisition and analysis.
- Simon White, Yipeng Sun, and Yngve Levinsen for help on computer problems and beam physics.
- John Jowett for interesting discussions on intrabeam scattering and tail repopulation.
- Francesco Cerutti for his insight on beam scraping studies for the LHC.

Bibliography

[1] P. A. Letnes et al., "Beam Scraping to Detect and Remove Halo in LHC injection,". Prepared for European Particle Accelerator Conference (EPAC 08), Genoa, Italy, 23-27 Jun 2007.

[2] H. Burkhardt *et al.*, "Beam scraping for LHC injection,". Prepared for Particle Accelerator Conference (PAC 07), Albuquerque, New Mexico, 25-29 Jun 2007.

[3] J. Gareyte, "Requirements of the LHC on its injectors," *Proceedings of Chamonix workshop IX* (1999) .

[4] H. Burkhardt and G. Arduini, "Transverse tail scraping in the SPS for clean LHC injection. Scraper Functional Specification," *CERN EDMS* (2006) .

[5] P. Collier, "Controlling the beam for extraction: Do we send it?," *Proceedings of Chamonix workshop XI* (2001) .

[6] P. Letnes, "Beam Scraping for LHC Injection: High Level Application Development," Tech. Rep. CERN-AB-Note-2008-012, CERN, Geneva, Mar, 2008.

[7] M. Facchini, C. Fischer, J. J. Gras, S. Hutchins, and R. Jung, "Scraping for LHC and collimation tests in the CERN SPS," Tech. Rep. CERN-AB-2005-070, Apr, 2005.

[8] W.-M. Yao et al., "Review of Particle Physics," *Journal of Physics G* **33** (2006) 1+. `http://pdg.lbl.gov`.

[9] M. Benedikt et al., "LHC Design Report, volume 3: the LHC Injector Chain," tech. rep., CERN, 2004.

[10] S. Y. Lee, *Accelerator Physics*. World Scientific, 1999.

[11] E. Courant and H. Snyder, "Theory of the alternating-gradient synchrotron," *Annals of Physics* **3** (1958) 1–48.

[12] H. Burkhardt and R. Schmidt, "Intensity and Luminosity after Beam Scraping," *CERN-AB-2004-032* (2004) .

[13] P. Bryant and S. Turner et al., *Cern Accelerator School 1984*. CERN Service d'information scientifique, 1984.

[14] V. Kain, J. Ramillon, R. Schmidt, K. Vorderwinkler, and J. Wenninger, "Material damage test with 450-GeV LHC-type beam,". Prepared for Particle Accelerator Conference (PAC 05), Knoxville, Tennessee, 16-20 May 2005.

[15] J. Allison et al., "Geant4 developments and applications," *Nuclear Science, IEEE Transactions on* **53** (Feb. 2006) no. 1, 270–278.

[16] S. Agostinelli et al, "Geant4 – a simulation toolkit," *Nuclear Instruments and Methods in Physics Research Section A: Accelerators, Spectrometers, Detectors and Associated Equipment* **506** no. 3, 250–303. (`http://www.sciencedirect.com/science/article/B6TJM-48TJFY8-5/2/23ea98096ce11c1be446850c04cfa498`).

[17] C. Carli, A. Jansson, and M. Lindroos, "A Comparative Study of Profile and Scraping Methods for Emittance Measurements in the PS Booster," Tech. Rep. CERN-PS-2000-062-OP, CERN, Geneva, Oct, 2000.

[18] G. Papotti, "A beam quality monitor for LHC beams in the SPS,". Prepared for European Particle Accelerator Conference (EPAC 08), Genoa, Italy, 23-27 Jun 2008.

[19] I. Reichel and M. Tonutti, *Study of the transverse beam tails at LEP. oai:cds.cern.ch:366331.* PhD thesis, CERN, Geneva, 1998. Presented on 3 Jul 1998.

[20] J. D. Bjorken and S. K. Mtingwa, "Intrabeam Scattering," *Part. Accel.* **13** (1983) 115–143.

[21] A. W. Chao and M. Tigner, *Handbook of Accelerator Physics and Engineering.* World Scientific, Singapore, 1999.

Dictionary and Symbol List

This appendix contains explanation of abbreviations and symbols used in this master thesis.

Symbol List

α

1. The Courant–Snyder parameter $\alpha = (-1/2)\mathrm{d}\beta/\mathrm{d}s$
2. α_c, the momentum compaction factor

β

1. Courant–Snyder parameter. Commonly referred to as betatron amplitude function, or just β function
2. Particle velocity divided by the speed of light, $\beta = v/c$

Φ Betatron phase advance

ϕ Particle RF phase relative to the synchronous particle

γ

1. The relativistic Lorentz factor
2. The Courant–Snyder parameter $\gamma = (1 + \alpha^2)/\beta$

μ The betatron phase advance for one turn

p_0 Design momentum

p_s Longitudinal particle momentum

p_x, p_y Transversal particle momenta

Q_x, Q_y (Linear) horizontal (x) and vertical (y) transversal tunes. The tune is the number of betatron oscillations per turn.

ν_x, ν_y (Linear) horizontal (x) and vertical (y) fractional transversal tunes. The tune is the number of betatron oscillations per turn.

Q'_x, Q'_y (Linear) horizontal (x) and vertical (y) transversal chromaticity ($\mathrm{d}Q/\mathrm{d}p$). The chromaticity is caused by momentum dependence of focusing effects in quadrupole magnets.

s The longitudinal particle coordinate

x, y Transversal particle coordinates

x_s, y_s Scraping position

Dictionary

Bunch The protons (or other particles) inside one RF bucket.

Coast Keeping the accelerator beam circulating at constant energy. Usually, the RF cavities are still active to keep the beam bunched.

Intensity In accelerator physics, the total number of particles in the beam.

Jaw The **jaw** of a collimator or a scraper is the physical object which touches the beam to remove particles from it

Quench A magnet **quench** occurs whenever a magnet is heated sufficiently to make the superconducting coils lose their superconductivity. This leads to electrical resistance, which in turn leads to more heating, and possibly an avalanche effect.

RF Radio Frequency, used for electromagnetic waves with frequencies of about 3 Hz–30 GHz.

RF Acceptance The (fractional) energy variation allowed for a particle, if the particle is not to be lost. The RF acceptance is equivalent to the height of the RF bucket.

RF Bucket The (stable) area in the longitudinal phase plane where particles are kept in the beam.

Super cycle A **super cycle** consists of a repeating pattern of one or more **user cycles**.

Turn One **turn** in a circular accelerator is one pass through the circumference of the ring.

User cycle A **user cycle** is the delivery of a beam with a given set of parameters to an experimental target or another accelerator. For instance, the SPS can have a super cycle consisting of two user cycles for injection of LHC beams.

Abbreviations

BLM Beam Loss Monitor

(E)PAC (European) Particle Accelerator Conference

ISR Intersecting Storage Rings, the world's first proton–proton collider, 1971–1984

LHC Large Hadron Collider

LINAC LINear ACcelerator

MAD-X Methodical Accelerator Design, version 10. Software written and used at CERN. See `http://mad.web.cern.ch/mad/`

MD Machine Development, experiment performed to learn more about the accelerator.

PS Proton Synchrotron

PSB Proton Synchrotron Booster

RF Radio Frequency

RMS Root Mean Square

SPS Super Proton Synchrotron

Scraper-related talks and meetings at CERN

- H. Burkhardt, "The use of the SPS scrapers during early LHC operation", LTC 27.04.2005, http://ab-div.web.cern.ch/ab-div/Meetings/ltc/ltc_2005-06a.pdf
- C. Fischer, "Final results on scraping in the SPS", APC 23.06.2005, http://ab-div.web.cern.ch/ab-div/Meetings/APC/2005/apc050623/minutes_050623.html
- H. Burkhardt, "SPS scraper MDs", APC 08.06.2006, http://ab-div.web.cern.ch/ab-div/Meetings/APC/2006/apc060608/HB-APC08-06-2006.pdf
- H. Burkhardt, "Measurements with the scrapers in the SPS", APC 13.04.2007, http://ab-div.web.cern.ch/ab-div/Meetings/APC/2007/apc070413/HB-APC-13-04-2007.pdf
- P. Letnes, "MDs with the Scraper at the SPS", APC 26.10.2007, http://ab-div.web.cern.ch/ab-div/Meetings/APC/2007/apc071026/PL-APC-26-10-2007.pdf
- P. Letnes, "Scraping in the SPS for LHC injection", ABP-LCU meeting 5.11.2007, http://ab-dep-abp.web.cern.ch/ab-dep-abp/LCU/LCU_meetings/2007/20071008/agenda.html
- P. Letnes, "Beam scraping at the SPS", Collimation Working Group meeting 04.02.2008, http://lhc-collimation.web.cern.ch/lhc-collimation/files/PLetnes_2008-02-04.pdf